Université de Montréal

Mechanical Study of Silicon Strip Detector Modules During Quality Control for the ATLAS Phase-II Detector Upgrade

par

Gabriel Demontigny

Département de Physique

Faculté des arts et des sciences

mars 2020

Université de Montréal

Faculté des études supérieures et postdoctorales

Ce mémoire intitulé

Mechanical Study of Silicon Strip Detector Modules During Quality Control for the ATLAS Phase-II Detector Upgrade

présenté par

Gabriel Demontigny

a été évalué par un jury composé des personnes suivantes :

Hugo Bouchard
_____
(président-rapporteur)

Jean-François Arguin
_____
(directeur de recherche)

Claude Leroy
_____
(membre du jury)

Mémoire accepté le :
3 février 2020
_____

Résumé

Suite à la détection du très attendu boson de Higgs, le Grand Collisionneur de Hadrons (LHC) ainsi que le détecteur ATLAS se prépare pour une importante mise à niveau. Prévu pour le LHC à Haute Luminosité (HL-LHC), le ITk (Inner TracKer), un trajectomètre pour particules chargées fait de silicium, est la mise à niveau du détecteur interne du détecteur ATLAS. Une phase de test des modules de détecteur du ITk est cruciale puisque le détecteur sera inaccessible pour environ 10 ans suite à l'installation. Ce mémoire se concentrera sur les tests effectués sur un sous-ensemble du détecteur ITk, soit le détecteur ITk Strip. Pour détecter les bris prématurés sur les 20 000 modules qui seront produits, une procédure de cyclage thermique sera mise en oeuvre, où les modules seront refroidis et réchauffés pour recréer les 10 ans d'opération. Ces tests seront effectués dans une enceinte appelé *coldbox*. Le thème de ce mémoire est le calcul du stress mécanique dans les modules ITk Strip induit par la procédure de cyclage thermique à l'aide de la méthode des éléments finis. Le premier résultat obtenu est que le stress induit dans le module installé dans le *coldbox* est causé par le vide appliqué sous le module pour le tenir en place. De plus, le stress maximal durant le cyclage thermique est grandement dépendant de l'épaisseur du joint sous-vide utilisé. Ainsi, un joint plus mince cause un stress plus faible. Finalement, le stress dans le *coldbox* est entre 20 MPa et 100 MPa variant avec l'épaisseur du joint, ce qui est en accord avec le stress calculé pour une disposition semblable au détecteur final, donnant un stress de 64.8MPa. Il est donc possible de conclure que le *coldbox* est un bon candidat pour effectuer le cyclage thermique.

Mot Clés: Physique des Particules, Détecteur ATLAS, Trajectomètre au Silicium, Méthode des Éléments Finis, Stress Mécanique

Abstract

Following the great achievement by the ATLAS experiment at the Large Hadron Collider (LHC) that is the detection of the long-awaited Higgs boson, an upgrade of the LHC is planned, requiring an upgrade of ATLAS. Planned for the High-Luminosity LHC, the ITk (Inner TracKer), an all-silicon charged particle tracker, is the upgrade of the current ATLAS Inner Detector. Testing of the detector modules comprised in the ITk is crucial because the detector will be inaccessible for approximately 10 years following the installation. In this thesis, the focus will be kept on a subset of the ITk detector, namely the ITk Strip detector. To detect premature failure in the 20 000 Strip modules that will be produced, a series of tests will be performed, one of which will be the thermal cycling, where modules are monitored while being thermally cycled to replicate 10 years of operating conditions. These tests will occur in a special enclosure known as a coldbox. The subject of this work is to study the induced mechanical stress in future ITk Strip detector modules due to thermal cycling using Finite Element Analysis. Our first result is that the stress created in the module is mostly due to the vacuum applied to hold the module. Moreover, the maximum stress felt during thermal cycling is highly dependent on the thickness of the vacuum seal used: A thinner seal causes a lower stress. Finally, the stress in the module in our thermal cycling setup is between ~ 20 MPa and ~ 100 MPa depending on the selected seal thickness, which is consistent with the stress expected in the final detector design which is approximately 64.8MPa. We can then conclude that the proposed design for the coldbox is a good candidate to perform thermal cycling.

Keywords: Particles Physics, ATLAS Detector, Silicon Tracker, Finite Element Analysis, Mechanical Stress

Contents

List of tables

List of figures

xvii

List of acronyms

Acronym	Meaning
ABC	Atlas Binary Chip
ALICE	A Large Ion Collision Experiment
AMAC	Autonomous Monitor and Control Chip
ASIC	Application Specific Integrated Circuit
ATLAS	A Torroidal Lhc ApparatuS
BSM	Beyond Standard Model
CMS	Compact Muon Solenoid
DM	Dark Matter
EC	End-Cap
ECAL	Electromagnetic CALorimeter
EM	ElectroMagnetism / ElectroMagnetic
EW	ElectroWeak
FEA	Finite Element Analysis
GUI	Graphical User Interface
HCAL	Hadronic CALorimeter
HCC	Hybrid Controller Chip
ITk	Inner TracKer
LHC	Large Hadron Collider
LINAC	LINear ACcelerator
PB	PowerBoard
PCB	Printed Circuit Board

Acronym	Meaning
PS	Proton Synchrotron
PSB	Proton Synchrotron Booster
QA	Quality Assurance
QC	Quality Control
QCD	Quantum ChromoDynamics
QED	Quantum ElectroDynamics
QFT	Quantum Field Theory
RF	Radio-Frequency
SCT	SemiConductor Tracker
SM	Standard Model of particle physics
SPS	Super Proton Synchrotron
SUSY	SUperSYmmetry

Acknowledgment

First of all, I want to thank my supervisor Jean-François Arguin, for his constant support and guidance throughout this project. He was always available and ready to help, which made this adventure orders of magnitude more enriching. I could not have hoped for a better supervisor.

I want to thank the entire ATLAS UdeM group for their help, even though i was working in a different building and what I was doing had nothing to do with their work, everyone was ready to help. I also want to thank the personnel from the Groupe Technologique.

I want to thank Martin Stegler, Filip Nechansky and Ingo Bloch from DESY in Germany, with whom I had the chance to work for this project. Ingo acted as my technical supervisor for my qualification task, and was very helpful for guiding my in me project.

On a more personal note, I want to thank my family, especially my parents, Josée and Alain, who supported me during my journey. I wouldn't have been able to do it if it wasn't for their help and counsel. They have always supported me, and I am forever grateful for that.

Introduction

Particle physics is the branch of physics that aims at the understanding of the universe at its smallest scale. The current best theory for describing particle physics is called the Standard Model of particle physics. This theory tries to explain every phenomenon in the universe in term of 12 fundamental matter particles called fermions and five force particles called bosons. Since its creation in the middle of the 20th century, the Standard Model predicted a number of new phenomena, such as the existence of the Higgs boson, theorized in the 1960's, finally discovered in 2012 by two separate experiments, ATLAS and CMS, at the Large Hadron Collider (LHC). Although the Standard Model makes incredibly accurate predictions, many problems are still present in this theory, and a new generation of experiment is needed to investigate these unanswered questions. An experiment from this new generation will be based on the upgraded ATLAS detector at the LHC.

The work presented in this thesis is on the mechanical study of silicon tracker modules for the upgrade of the ATLAS detector at the LHC. Due to the size of the ATLAS detector, upgrading this apparatus is a tremendous task, and has to be done in the most careful way, hence a thorough testing procedure for the modules making the final apparatus is crucial. Because some of the test performed on these modules are particularly harsh, for example thermal cycling of modules, a deep understanding of the stresses involved in these tests is very important. This thesis will present simulations computing the stress in the sensor of the aforementioned detector modules caused by the thermal cycling procedure, as well as various investigations done.

In chapter 1, the basics of the Standard Model of particle physics will be presented, going over the different fundamental particles and the forces governing them. A quick overview of a few theories beyond the Standard Model will also be covered, justifying the interest in looking for new signatures in particles physics. Finally, a basic summary of a promising theory beyond the standard model will be given, namely Supersymmetry, which is one of the main focus of the particle physics group here, at Université de Montréal.

In chapter 2, an introduction to the basics of experimental particle physics will be given, introducing the concept of particle accelerators and particle detectors. A few examples as well as the basic workings of these instruments will be presented. This will be followed by the presentation of the current largest and most powerful particle accelerator in the world, the LHC. The four main detectors installed at this facility will also be described, with an emphasis on the ATLAS detector. Finally, the project to upgrade the current ATLAS detector will be briefly presented, highlighting the reasons for this upgrade.

In chapter 3, the upgrade of the ATLAS detector will be presented in greater detail, especially the Inner Tracker (ITk), which is the topic of this work. The ITk Strip detector will be presented, which is a part of the ITk, highlighting it design and building. The following part is a description of the testing procedure of these detector modules, presenting the two different approaches, namely Quality Control and Quality Assurance. Next, thermal cycling of modules, which is one of the most important tests of both quality control and quality assurance, will be described, as well as the setup needed to perform it and the main challenges encountered during the preliminary tests.

Finally, in chapter 4, following the challenges of thermal cycling, a mechanical study of detector modules during thermal cycling will be presented. First, a quick introduction to Finite Element Analysis (FEA) will be given. Then, an overview of the software, procedure, and materials used for the FEA simulation will be described. Finally, the results of the various mechanical simulations will be presented for every situation studied, namely, a free module, a module on the thermal cycling setup with

only the vacuum applied, the same setup now with cooling and heating, a study of the impact of vacuum seal thickness on the stress, an investigation of vacuum failure, and finally the stress in the module in a configuration similar to the final detector. In this section, the different geometries and particularities of the simulations will be described in greater details.

Chapter 1

Theoretical Context

In this chapter, the Standard Model of particle physics will be described. The different matter particles will be presented as well as the force-mediating particles, to give the reader a general understanding of the most fundamental physics currently discovered. The differences between both type of matter particles will be explained with their respective forces by which they interact. The unification of two of the three forces included in the SM will be briefly explained, as well as the mechanism giving the mass to the SM particles. Finally, a few problems of the SM will be given, with a possible theory explaining these phenomena.

1.1. Standard Model of Particle Physics

The Standard Model of Particle Physics (SM) is the most fundamental theory of the universe yet discovered. This theory is based on Quantum Field Theory, which constitutes the study of quantized fields. In the SM, matter is made of spin-1/2 particles called fermions, while force-mediating particles are of integer spin (S=0, 1), called bosons. These particles are described by the statistical distribution of Fermi-Dirac and Bose-Einstein, respectively. Figure 1.1 shows a representation of the particles included in the SM with some of their properties [1].

1.1.1. Bosons

The bosons are separated into two categories: the gauge bosons, which are spin-1 particles and a scalar boson, which is spin-0. There are 12 gauge bosons that are
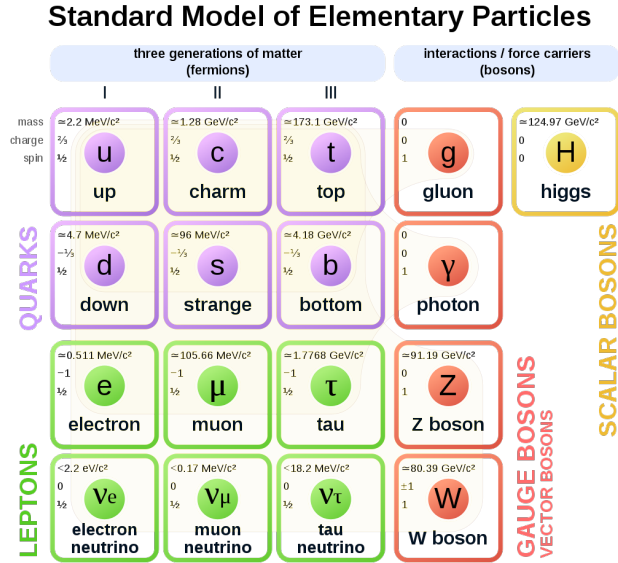
Fig. 1.1. Representation of the Standard Model of Particle Physics.

carrying the three different forces of the SM. First the photon (γ) carrying the electromagnetic (EM) forces and interacting with the electric charge, then the W^+, W^- and Z bosons carrying the weak nuclear force interacting with the weak isospin and finally eight gluons (g) carrying the strong nuclear force interacting with color (will be explained later). The only scalar boson in the SM is the Higgs boson. The role of the Higgs boson, and its associated field, is to give mass to the other particles of the SM. Note that gravity is not included in the SM and this leads physicists to believe that the SM is not the absolute theory of the universe.

1.1.2. Fermions

The fermions are separated into two classes, the quarks and the leptons. Both classes of fermions are arranged into three generations. The first generation contains the fermions that make the normal matter, i.e. the up and down quarks (making protons and neutrons) as well as the electron and its associated neutrino. The two other generations of fermions are simply a heavier copy of the first. Fermions from higher generations are much less abundant in the universe because they will decay relatively quickly to lighter fermions until they reach the first generation, where decay

is prohibited by conservation of quantum number. Nonetheless, every generation of fermion can be created with an energetic enough event, or by flavor oscillation for the neutrinos [2]. For massive fermions, the spin can be aligned or anti-aligned with respect to the direction of propagation of the particle. This is defined as the helicity of the particle, right-handed (R) is when the spin is aligned with the direction of propagation, while left-handed (L) is for particles with spin anti-aligned with the direction of propagation. The helicity of a particle can be changed by changing the frame of reference to invert the direction of propagation of the particle, right-handed particles then become left-handed. Another similar concept is present in the SM, which is called chirality. Chirality is an intrinsic quantum property of every particle, having two different values: right-chiral or left-chiral. The distinction between helicity and chirality is crucial as the SM interacts differently with particles of different chirality, namely, chirality is an intrinsic property of particles and helicity refers to the relative orientation of the spin of a particle to its momentum (right-helicity particles have their spin parallel to their momentum and left-helicity particles have their spin opposite to their momentum).

1.1.2.1. *Quarks*

The quarks are fermions that interact via every force of the SM. Because they interact by the strong force, they are confined to exist inside composite particles called hadrons. Hadrons can be made of a quark-antiquark pair (mesons) or three quarks (baryons). The first generation of quarks contains the up (u) and down (d) quarks, which are the building blocks of the nucleus of atoms, i.e. protons and neutrons are baryons made of a combination of "u-u-d" and "u-d-d" quarks respectively. The higher generations are made of the charm (c) and strange (s) quarks as well as the top (t) and bottom (b) quarks. For all generations, the *up-like* quarks (u-c-t) are of electric charge $q = +2/3$ and the *down-like* quarks are of electric charge $q = -1/3$. In the SM, the top quark is the heaviest particle (≈ 173 GeV [3]), which makes it a good candidates to study the Standard Model at the LHC.

1.1.2.2. *Leptons*

Leptons are fermions that interact by the weak nuclear force and the EM force. The first generation of lepton contains the electron (e^-) and its associated neutrino (ν_e). As it is well known, electrons are found "orbiting" the nucleus of atoms, giving them their chemical properties. Moreover, electron neutrinos are abundantly produced by nuclear reaction in all stars, when nuclear fuel is consumed. The higher generations of leptons are the muon (μ^-) and muon neutrino (ν_μ) as well as the tau (τ^-) and tau neutrino (ν_τ). In the SM, neutrinos only have a left-chiral component, and were believed to be massless. This was refuted when neutrino flavor oscillation was observed, since flavor oscillation is only possible for massive particles [4], although the origin of their mass is uncertain. This discovery led to a Nobel Prize in Physics to Prof. Arthur B. MacDonald and Prof. Takaaki Kajita in 2015.

1.1.3. Electromagnetic Force

The EM force is described by Quantum Electro Dynamic (QED), the quantum field theory (QFT) for the photon and fermions with an electric charge. QED is represented by the $U(1)$ group which has a single generator, hence only one gauge boson for this interaction. Because the photon is massless, the EM force has an infinite range. Figure 1.2 shows the basic Feynman diagram for the QED vertex, representing the interaction of two fermions with a photon. Note that for every Feynman diagram in this work, it is assumed that the spatial coordinate is upward, and increasing time goes to the right.
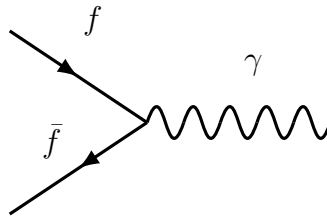
Fig. 1.2. Basic vertex of QED showing the interaction of two fermions with a photon.

1.1.4. Weak Force

The Weak force is represented by the $SU(2)_L$ group which has 3 generators, hence it has 3 force carriers, the $W^\pm$ bosons as well as the Z boson. The "charge" for this interaction is called weak isospin (I). The "L" in $SU(2)_L$ represents the chirality of the fermions. Left-chiral particles are in a doublet of isospin ($I = 1/2$) while right-chiral particles are in a singlet of isospin ($I = 0$). Thus only left-chiral fermions are sensitive to the weak force. In the SM, the left-chiral up-like quarks (u c t) and charged leptons (e^- μ^- τ^-) have their 3rd component of weak isospin I_3 equal to $I_3 = +1/2$ while the down-like quarks (d s b) and neutrinos have $I_3 = -1/2$. For anti-particles, the weak isospin is opposite. In the weak theory, gauge bosons have isospin $+1$, 0 and -1 for the W^+, Z and W^- respectively. Because weak isospin is conserved, a $+1/2$ I_3 fermion can be changed to a $-1/2$ I_3 fermion by the exchange of the appropriate W boson. However leptons and quarks cannot be mixed because of leptonic and hadronic number conservation. The three basic weak interaction vertices are presented in figure 1.3.
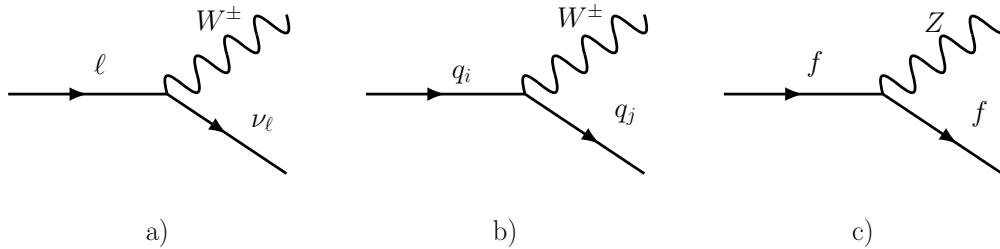
Fig. 1.3. Basic vertices of the weak force showing the interaction of two fermions with vector bosons. a) Charged current changing a charged lepton into a neutrino. b) Flavor-changing charged current. c) Neutral current.

1.1.5. Electro-Weak Unification

The electroweak (EW) force is the unification of the electromagnetic and Weak nuclear force in the Standard Model. It is represented by the group $SU(2)_L \times U(1)_Y$, generated by two quantum numbers, the weak isospin I for $SU(2)_L$ and the weak

9

hypercharge Y_W for $U(1)_Y$. In the EW theory, the weak hypercharge is defined as $Y_W = 2(Q_{EM} - I_3)$ with Q_{EM} being the traditional electric charge and I_3 the 3$^{\text{rd}}$ component of isospin, as defined in section 1.1.4. This theory has four physical vector bosons, that are made of combinations from the vector bosons of the $SU(2)_L$ group $(W_\mu^1, W_\mu^2, W_\mu^3)$ and $U(1)_Y$ group (B_μ). The physical $W^\pm$, Z and γ, are given by equation 1.1.1,

$$
\begin{aligned}
W_\mu^\pm &= \frac{1}{\sqrt{2}}(W_\mu^1 \pm iW_\mu^2)\,, \\
Z_\mu &= \cos\theta_W B_\mu + \sin\theta_W W_\mu^3\,, \\
A_\mu &= -\sin\theta_W B_\mu + \cos\theta_W W_\mu^3\,.
\end{aligned}
\tag{1.1.1}
$$

where $W_\mu^\pm$ and Z_μ are simply the $W^\pm$ and Z boson, and A_μ is the photon (γ).

1.1.6. Strong force

The strong force is described by Quantum Chromodynamic (QCD), and is represented by the $SU(3)$ group which has eight generators, hence eight carriers, the gluons. The "charge" for this interaction is called "color", and it has three different values: Red (r), green (g) and blue (b). Every quark has a color, every anti-quark has an anticolor ($\bar{r}$, $\bar{g}$ and $\bar{b}$) and each one of the eight gluons possess a combination of a color and an anticolor. It is believed that to be able to exist freely, a particle has to be a color singlet, meaning that it either has to be a color-anticolor pair ($r\bar{r}$, $g\bar{g}$ or $b\bar{b}$) or every color or anticolor (rgb or $\bar{r}\bar{g}\bar{b}$). This is called the color confinement hypothesis. This explains why the only free baryons observed are mesons ($q\bar{q}$) and hadrons (qqq)[1]. In QCD, the gluons also carry both a color and an anti-color, figure 1.4 shows a representation of the eight physical gluons of QCD, where Y^C and I_3^C are the color hypercharge and 3$^{\text{rd}}$ component of color isospin, respectively. These two quantities are the color equivalent of the weak hypercharge (Y_W) and the weak isospin (I_3), respectively.

---

[1]A recent paper claims the discovery of a pentaquark [5], but it is unclear if it is made of 5 strongly coupled quarks ($qqqq\bar{q}$), or composed of a weakly bounded meson-hadron pair ($q\bar{q}$-qqq), so it is not going to be considered in this work.
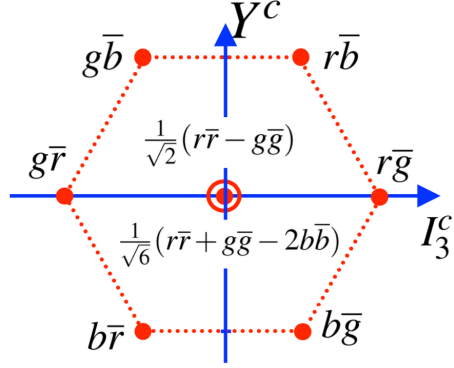
Fig. 1.4. Isospin-Hypercharge diagram of the strong force, displaying the eight physical gluons and their respective color combination.

Because gluons carry color, they can interact with themselves, creating three-gluons and four-gluons interactions. This is thought to be the cause of color confinement. When two quarks are separated, more gluons are created due to self-interaction, which increases the energy of the quark-quark bond. After a certain distance, it is more energetically favorable to create a quark-antiquark pair and break the original bond, rather than to keep increasing the energy. This behavior can be expressed as a potential proportional to the distance between the quarks, as shown in equation 1.1.2.

$$V_{QCD}(r) \sim \lambda\, r\,. \tag{1.1.2}$$
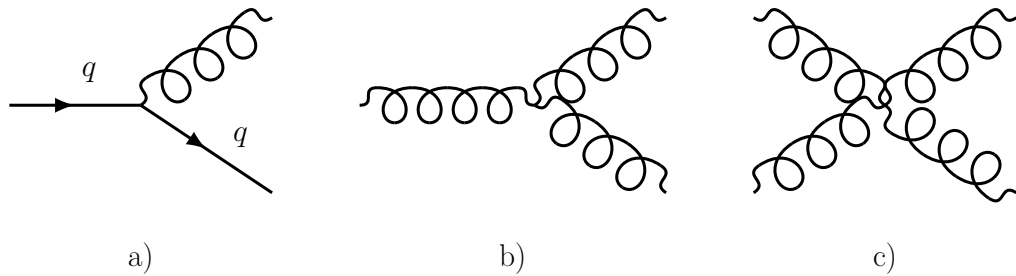
Fig. 1.5. Basic vertices of the strong force showing a) the interaction of two quarks with a gluon, b) Three-gluon interaction, c) Four-gluon interaction.

1.1.7. Higgs Boson

In the Standard Model, the neutral part of the Higgs is a complex scalar field with a potential in the form of equation 1.1.3 [6].

$$V(\phi) = \mu^2(\phi^*\phi) + \lambda(\phi^*\phi)^2. \qquad (1.1.3)$$

If $\lambda > 0$ and $\mu^2 < 0$ then the potential has a characteristic "Mexican hat" shape, with minima at $v = \sqrt{\frac{-\mu^2}{\lambda}}$. Because the minimum is not a single point, it forces the field to "choose" a value which is called a vacuum expectation value (vev), causing spontaneous symmetry breaking of the Lagrangian. The above parameters are experimentally estimated to be $\lambda \approx 0.126$ and $\mu^2 \approx -(92.9\text{GeV})^2$. Because the Higgs field has a non-zero vev, the SM particles are continuously interacting with it, adding a mass term to their Lagrangian. The Higgs field excitation is called the Higgs boson, and it was theorized in 1964 by Peter Higgs and Francois Englert, only to finally be observed in 2012 by the ATLAS and CMS experiments at the LHC.

A thorough description of the Higgs mechanism is given in the textbook *Modern Particle Physics* by Mark Thomson [6]. It will give the reader a much deeper understanding of this phenomenon.

1.1.8. Summary of the Standard Model

As described in the previous sections, the SM is a very elegant theory, able to predict the vast majority of what is being observed in the universe. Figure 1.6 shows a summary of the total production cross section of several SM processes, as well as their comparison with theoretical expectations [7]. It is clear that the SM agrees incredibly well with experiment for these processes, even though some really important questions cannot be answered by this theory. It is then clear that the SM is not the absolute theory of particle physics.

1.2. Beyond the Standard Model

In the previous section, the Standard Model of particle physics was introduced. Although this theory is able to explain to an impressive accuracy certain aspect of the

Standard Model Total Production Cross Section Measurements — Status: March 2019

ATLAS Preliminary

Run 1,2 $\sqrt{s}$ = 7,8,13 TeV

$\int \mathcal{L}\, dt\ [fb^{-1}]$ — Reference

Row labels: pp, W, Z, $t\bar{t}$, t_{t-chan}, WW, H, Wt, WZ, ZZ, t_{s-chan}, $t\bar{t}W$, $t\bar{t}Z$, tZj, WWW, WWZ

Legend: Theory; LHC pp $\sqrt{s}$ = 7 TeV (Data, stat, stat ⊕ syst); LHC pp $\sqrt{s}$ = 8 TeV (Data, stat, stat ⊕ syst); LHC pp $\sqrt{s}$ = 13 TeV (Data, stat, stat ⊕ syst)

Axis labels: σ [pb]; data/theory
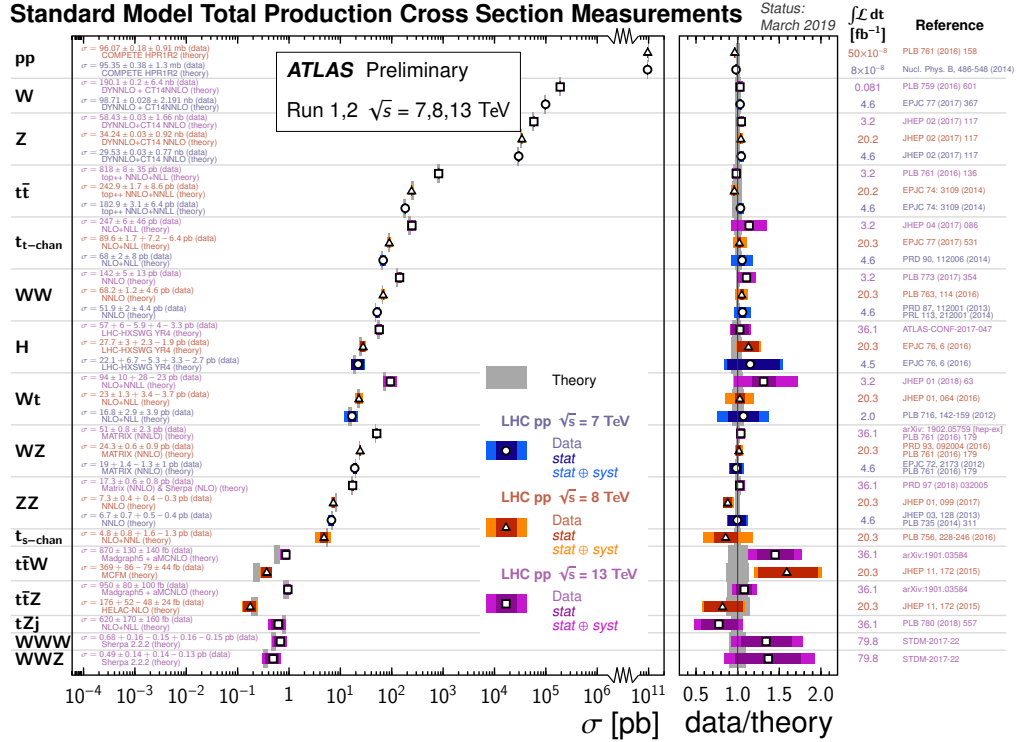
Fig. 1.6. Summary of several Standard Model total production cross section measurements, corrected for leptonic branching fractions, compared to the corresponding theoretical expectations and ratio with respect to best theory.

universe, such as the fine-structure constant and the anomalous magnetic moment of the electron [8], there are some questions in physics that this theory still isn't able to answer. Some problems of the SM will be addressed in this section, as well as a few theories that try to solve these problems.

1.2.1. Problems with the Standard Model

Despite its incredibly precise predictions, the SM isn't able to solve all problems in current particle physics. Some of these problems are the followings: the fine-tuning problem, the existence of dark matter, the matter/anti-matter asymmetry of the universe and the addition of gravity.

1.2.1.1. *The Fine-tuning Problem*

The fine-tuning problem comes from the fact that the EW energy scale is highly dependent on the top quark Yukawa coupling. To be able to match the W boson mass, the value of the top quark mass has to be tuned to about 0.3 MeV ($m_t \approx 173$ GeV), which is a tuning of about two part in a million [9].This fine tuning is also a problem for the Higgs boson which couples to every massive particles of the SM, meaning that its mass receives correction from the most massive particle of the SM. Such fine-tuning is unnatural, which pushes physicist to think that there might by physics beyond the Standard Model that can account for this phenomenon.

1.2.1.2. *The existence of Dark Matter*

Dark matter (DM) is a kind of matter that accounts for approximately 85% of the entire mass content of the universe. Through observation, it is thought that DM is interacting only by gravity and possibly the Weak interaction, which makes its observation very challenging. The first evidence of dark matter was noticed by Physicist Frank Zwicky in the beginning of the 1930's when he was observing redshift of nebulae in the Coma Cluster [10]. He noticed a much higher velocity dispersion than expected. With calculations, he established that the total mass of the galaxies contained in the cluster were roughly 1/400 the mass necessary for the rotational speed observed, meaning that the remaining mass is dark matter. Since then, numerous other observation proved the presence of DM in the universe by its gravitational effect, unfortunately no other direct detection has been made [11].

1.2.2. Supersymmetry

Supersymmetry (SUSY) is a theory beyond the standard Model that adds a symmetry between bosons and fermions. In fact, the basic principle of SUSY is that each boson (fermion) will have a fermionic (bosonic) superpartner. This idea is very interesting because due to the nature of the superpartner, their contribution to the mass of the Higgs boson will cancel out because bosons and fermions have opposite contribution [12]. Hence, if there exists a superpartner for every particle in the SM,

the fine tuning problem would be naturally explained by SUSY. Figure 1.7 shows the Minimal Supersymmetric Standard Model (MSSM) table, with SM particles on the left side and their SUSY partner on the right [13].
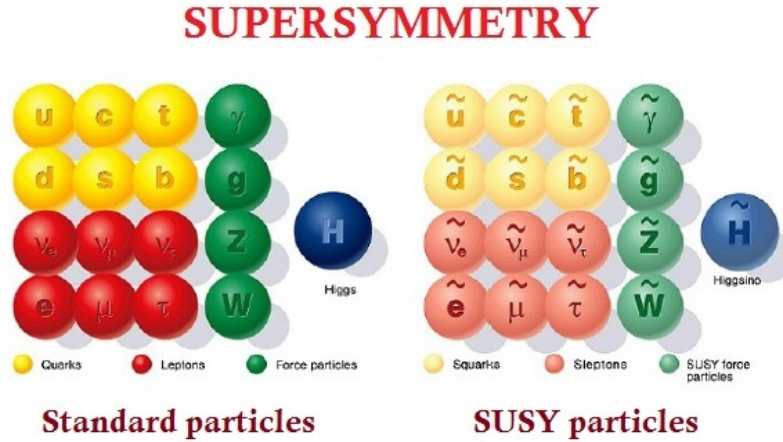
Fig. 1.7. Representation of the particles of the Minimal Supersymmetric Standard Model

In MSSM, the neutral Higgsinos ($\tilde{H}_u^0$ and $\tilde{H}_d^0$) and neutral gauginos ($\tilde{W}^0$ and $\tilde{B}$) will mix due to EW symmetry breaking to created four mass eigenstates, called neutralinos [12], usually denoted $\tilde{\chi}_n^0$. The lightest neutralino ($\tilde{\chi}_1^0$) is thought to be the lightest supersymmetric particle, and is a promising candidate for dark matter. Since SUSY seems to have answers to some of the most important problems in modern particle physics, a lot of effort is put into searching for its signature in high energy physics experiment. One such experiment is ATLAS at the Large Hadron Collider (LHC). Figure 1.8 show a summary of the search for SUSY at the ATLAS experiment, displayed as mass limit on the supersymmetric partner of known particles [14].

ATLAS SUSY Searches* - 95% CL Lower Limits
March 2019

ATLAS Preliminary
$\sqrt{s}$ = 13 TeV

*Only a selection of the available mass limits on new states or phenomena is shown. Many of the limits are based on simplified models, c.f. refs. for the assumptions made.
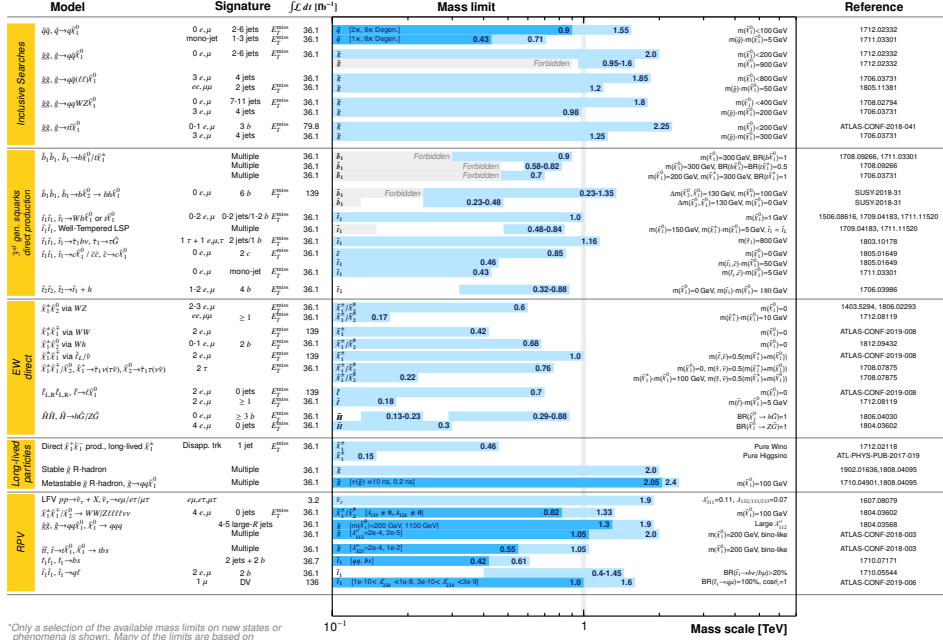
Fig. 1.8. Mass reach of the ATLAS searches for Supersymmetry. A representative selection of the available search results is shown. Results are quoted for the nominal cross section in both a region of near-maximal mass reach and a demonstrative alternative scenario, in order to display the range in model space of search sensitivity. Some limits depend on additional assumptions on the mass of the intermediate states, as described in the references provided in the plot. In some cases these additional dependencies are indicated by darker bands showing different model parameters.

Chapter 2

Experimental Context

In this chapter, the basics of particle accelerators for high energy physics will be presented in section 2.1, summarizing two of the main accelerating techniques. Then, the working of particle detectors will be described in section 2.2, presenting the two main kind of detectors. Then the Large Hadron Collider will be presented in section 2.3, with a summary of the main experiments taking place on the accelerator complex in section 2.3.2. Afterwards, the ATLAS experiment will be described in greater details, covering the main subdetectors comprised in the ATLAS apparatus in section 2.4. And finally the High-Luminosity LHC project will be described in section 2.5, with the intended increase in luminosity.

2.1. Particle Accelerator

2.1.1. Basics of particle accelerators

The workings of particle accelerators can be simply explained by classical electrodynamics. In fact, the two main ideas behind accelerators is that a charged particle in an electric field will be accelerated, and that a moving charged particle in a magnetic field will be accelerated in such a way that its path will form a helix. This behavior is described by the Lorentz force, written as equation 2.1.1.

$$\vec{F} = q(\vec{E} + \vec{v} \times \vec{B}).$$
(2.1.1)

The first term of equation 2.1.1 represents the force parallel to the electric field (E), while the second term represents a force caused by the magnetic field that is perpendicular to both the magnetic field and the velocity of the particle, hence the helix motion. This motion can be separated in a motion with constant velocity parallel to the magnetic field plus a circular motion "around" that same magnetic field. The circular motion is described by a radius given by equation 2.1.2, where γ is the Lorentz factor from special relativity and $v_\perp$ is the component of the velocity perpendicular to the magnetic field.

$$r = \frac{\gamma m v_\perp}{|q|B} \, . \tag{2.1.2}$$

With these two very simple concepts, a basic particle accelerator can be created, and the accelerated bunches of particles can be collided to create a particle collider such as the LHC. An important parameter of a particle collider is its luminosity, denoted by $\mathcal{L}$ in $\mathrm{cm}^{-2}\mathrm{s}^{-1}$ (integrated luminosity is also used where $\mathcal{L}$ is integrated over a certain period of time), which represents how well the accelerator can collide particles. Luminosity is a function of the parameters of the accelerator itself, as given by equation 2.1.3, where f if the frequency of bunch crossing, N_1 and N_2 are the number of particles in each bunch, and σ_x and σ_y are the transverse size of the beams. It is related to the rate of interaction by equation 2.1.4, where σ is the cross section of the desired interaction.

$$\mathcal{L} = \frac{fN_1 N_2}{4\pi\sigma_x \sigma_y} \, , \tag{2.1.3}$$

$$R = \sigma\mathcal{L} \, . \tag{2.1.4}$$

These concept are general for any kind of accelerator, but the workings of real accelerators depend on their nature. In subsections 2.1.2 and 2.1.3, two different kinds of particle accelerators used at the LHC will be discussed, explaining the particularities of each one.

2.1.2. Linear Accelerators

Linear accelerators (LINACs) are the starting point of many modern particle accelerators. They use Radio-Frequencies (RF) to create alternating electric field

that will accelerate the particles. Figure 2.1 shows a drawing of such an accelerator [15]. The LINAC is made of a vacuum chamber with aligned cylindrical tubes inside it. These tubes are made of an electrically conducting material, such as copper, thus creating a resonant cavity with the RF-field applied. This whole apparatus is also called a klystron. The tubes in the klystron are connected to a RF generator to apply an alternating electrical potential to accelerate the charged particles. The frequency of the RF generator is selected in such a way that it matches the frequency of particles passing the gap between the tubes. While particles are inside the tubes, they are shielded from the electric field, and only get accelerated when they cross the gap. Once passed the gap, the polarity is inverted due to the RF generator, so the particles are re-accelerated in the following gap. This process is repeated until the particles exit the klystron, with particles gaining energy every time they cross a gap.
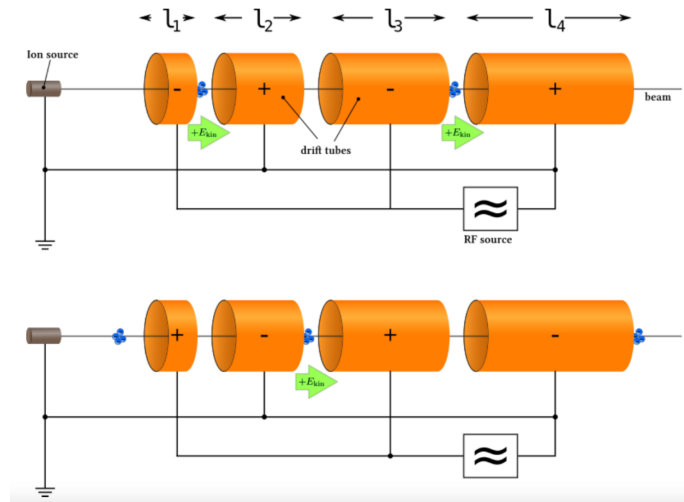
Fig. 2.1. Representation of a drift tube linear accelerator. Drift tubes of varying lenght are connect to an RF generator to create the accelerating E-field.

This process will naturally create bunches of particles accelerated together, because they need to be in phase with the RF signal to be properly accelerated. This bunch generation is crucial for colliders because the collisions can be controlled to occur at a specific position and time.

2.1.3. Synchrotron Accelerator

The synchrotron accelerators are the main part of the LHC. They are used to create the bunches of protons, and to accelerate them from 50 MeV to 13 TeV in 4 stages. The main idea behind Synchrotron is that a single pass in a klystron can only give a limited amount of energy to a bunch. With dipole magnets, the trajectory of the bunch is then modified so the particles pass multiple times in the same klystron, increasing their energy every time. If the energy of the particles is of the order of their mass, or smaller, their speed as well as their mass will increase (due to special relativity). Because of that, the magnetic field of the dipole magnets as well as the frequency of the RF generator has to be modified, to account for the variation of the radius of curvature of their trajectory, as in equation 2.1.2. If the energy of the particles is much greater than their mass, then only the magnetic field has to be modified as their speed approaches the speed of light. Because the accelerator's properties have to be modified synchronously to the beam's properties, these accelerators are called synchrotron. Figure 2.2 shows a diagram of a typical collider using a synchrotron. Because the beam of particles stays longer in the accelerator, quadrupole magnets are added to focus the beam, as a lens would do for optical beams.

Once the particles have reached the desired energy, two beams can be collided at the site of a specifically designed detector to look for new physics. This technique is how the LHC is working, collecting the products of 13 TeV proton-proton collisions in the four main detectors installed on its main synchrotron. The basic principles of particle detectors will be described in section 2.2.

2.2. Particle Detectors

Detectors in particle physics can follow two general principles: tracking and calorimetry. For tracking, detectors are designed to interact as little as possible with the incoming particles. The purpose of such detectors is only to measure where a particle passed and to reconstruct its trajectory. As for calorimetry, the detectors
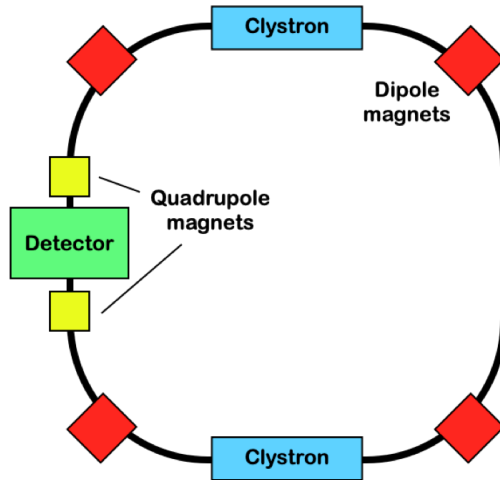
Fig. 2.2. Representation of the main ring of basic synchrotron collider. The klystrons are shown in blue, dipole magnets for bending the beam are represented in red, quadrupole magnets for focusing are in yellow and a particle detector is represented in green.

are designed to interact as much as possible with the particles, even stopping them in the volume of the detector, to be able to measure their position and energy. Section 2.2.1 and 2.2.2 will give a summary of a few different technologies used for tracking and calorimetry.

2.2.1. Trackers

There exists dozens of different technologies for particle tracking that were used since the beginning of the 20$^{\text{th}}$ century. some of the oldest are emulsion plates, which are similar to photographic plates, and bubble chambers, which are vats of super-heated liquid that boil when a particle passes through. The most common detectors used for tracking nowadays will be described in the following paragraphs, starting with wire chambers and then solid-state trackers.

Wire chambers have very simple design, they are made of a volume filled with gas with wires arranged in different patterns. The wires are held at high electrical potentials, causing electrons to drift towards them when a particle passes through the detector and ionizes the gas. The position of the wire on which the current is collected

gives a measurement of the position of the particle. The timing of the incoming signal can also be used to infer the position of the track with greater accuracy. A wide range of possible voltages can be used to run these detectors, ranging from proportional mode, Geiger mode to discharge mode. Figure 2.3 shows the collected charge as a function of the applied voltage [16]. In proportional mode, the charges created by the passage of ionizing radiation is proportional to their energy deposition. In Geiger mode, the charge deposited is independent of the radiation's energy deposition, as well as the voltage used, while in discharge mode, the charge is only dependent on the voltage used, due to ionization cascade because the voltage re-accelerates the electrons, creating more charges.
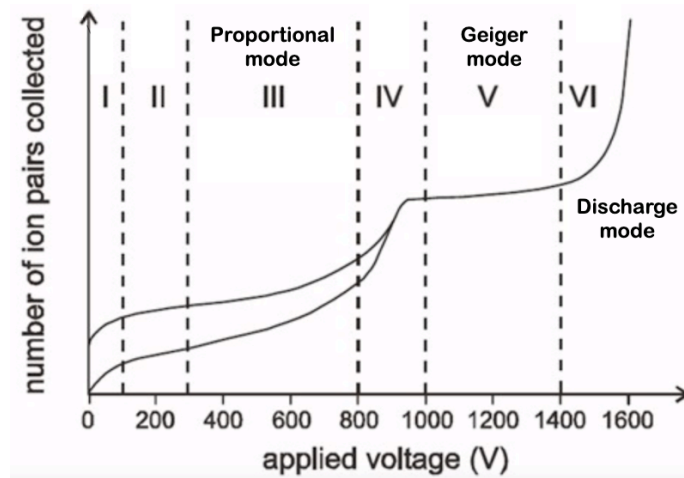
Fig. 2.3. Number of electron-ion pairs collected as a function of the applied voltage for ionizing detectors, showing the different modes (Proportional, Geiger, Discharge). The two curves represent two different particle's energy deposition.

Solid-state tracker are often based on semiconductor. This category of material has a very small electron band gap. This means that with a small amount of energy, a bound electron can be transferred into the conduction band, where it will be able to create a current. The most common semiconductor used in particle detectors are silicon and germanium crystals, having band gap energies of approximately 1.14 eV and 0.67 eV respectively. Although germanium has a smaller band gap, silicon is usually used for big scale experiments due to its low cost, lower density, and its higher

operating temperature, usually room temperature. Semiconductor trackers work similarly to wire chambers, meaning that particles pass through and deposit a small amount of energy. This energy, instead of ionizing a gas, actually creates electron-hole pair in the bulk of the semiconductor, which will drift towards electrodes due to a voltage applied across the detector. The current created on a specific electrode of this detector give the position of the track made by the particle.

If coupled with a magnetic field, a tracking detector can give a measurement of the momentum of a particle (assuming $q = \pm 1$) because the radius of the trajectory is proportional to the momentum, as well as inversely proportional to the applied magnetic field and charge of the particle, as seen in equation 2.1.2. Since only the tracks of particles with electric charge will bend in the presence of a magnetic field, another method is needed to detect electrically neutral particles. One such method, called calorimetry, uses special detectors called calorimeters to achieve a proper measurement of neutral particles as well as providing an additional measurement for charged particles.

2.2.2. Calorimeters

In the context of particle physics, calorimeters are detectors built and designed to interact as much as possible with the incident particles so that it can deposit its entire energy in the detector's active volume. There exists two main technologies for calorimeter: Sampling and homogeneous calorimeters.

Sampling calorimeters, are built with stacked layers of two different materials, one acting as absorber and the other as active material. The main purpose of the absorber is to interact with the incoming particles and create showers of secondary radiation. the nature of this material can vary depending if the calorimeter is aiming to detect electromagnetic particles (electrons, positrons and photons) or hadrons (bound states of quarks). Usually, the absorber is made of a dense material such as lead or steel, because of their high mass number (Z), they have higher cross section for such interactions. The active materials in sampling calorimeters are usually scintillating materials, such as plastic or crystal scintillators, or noble liquids. The

amount of light produced by these detectors is proportional to the energy deposited in them. Unfortunately, this energy is only a fraction of the total energy of the shower, due to the interaction with the absorber, which worsens the energy resolution of the sampling calorimeter. Nonetheless, this technology can be easily segmented laterally and longitudinally, giving a good shower position resolution.

Homogeneous calorimeters, as the name implies, are made of a single material, acting both as absorber and active material. Because a single material is used both as absorber and active material, it is advantageous to have a scintillator with high atomic number "Z" to have a sufficient cross section for interactions, but also a high enough light yield for a good energy resolution. In the context of high energy physics and collider physics, it is advised to use inorganic scintillating crystals, because of their higher mass number as well as their higher light yield compared to organic plastic scintillators. Although inorganic scintillators' properties are better suited for homogeneous calorimeters, it is difficult and expensive to produce large crystals with high purity. Nonetheless, because all the energy is deposited in active materials, this kind of calorimeter has a higher energy resolution compared to sampling calorimeters.

Multiple techniques can be used to identify the products of high energy collisions. for example, one can measure the energy and momentum of the produced particles via calorimeters and track curvature respectively. One can also use the time-of-flight or the energy deposition as a function of depth (also referred as dE/dx) to infer the velocity of the particles. Finally, the detectors in which the particles interact can give an indication of the nature of the particles, for example if it has an electrical charge or if it can interact via the strong force. These techniques are used in many experiments, such as those held at the Large Hadron Collider, to precisely determine the products of proton-proton collisions at 13 TeV. This huge infrastructure will be discussed in section 2.3, as well as the different experiments taking place at this particle collider.

2.3. Large Hadron Collider (LHC)

The Large Hadron Collider (LHC) is the largest and most powerful particle accelerator in the world, located at the border between France and Switzerland. The main accelerator has the shape of a ring of 27 km of circumference, located in an underground tunnel approximately 175 m underground. This accelerator can collide beams of protons at an energy of 13 TeV (two opposite beams of 6.5 TeV) with an instantaneous luminosity of $2 \times 10^{34}\text{cm}^{-2}\text{s}^{-1}$. To achieve such a task, the LHC uses more than 1200 dipole magnets to bend the trajectory of the beams, keeping it on a quasi-circular path, and almost 400 quadrupole magnets to focus the beam. Along the LHC, there are four points where the beams are crossed, creating collisions. These four points are the locations of the four main experiments of the LHC: ATLAS, CMS, ALICE and LHCb. An overview of the accelerator complex will be given in section 2.3.1, Then the experiments will be discussed in section 2.3.2.

2.3.1. Accelerator Complex

The LHC is an accelerator complex, made of several individual accelerator of different nature, combined together to create the biggest accelerator in the world. Figure 2.4 shows a drawing of the 6 main accelerators [17], starting with 2 linear accelerators (LINAC), one for protons (marked as "p" for proton) and one for heavy ions (marked as "Pb" for lead). The LINAC for protons accelerates them to a kinetic energy of 50 MeV. Then the accelerated particles are sent to the first synchrotron accelerator, called the Proton Synchrotron Booster (PSB, but unmarked on figure 2.4) where protons reach a kinetic energy of approximately 1.4 GeV. The following accelerator is called the Proton synchrotron (PS) and accelerates protons to a kinetic energy of 26 GeV. Once they exit the PS, protons are headed to the Super Proton Synchrotron (SPS) where they reach a kinetic energy of 450 GeV. Finally, the protons reach the main ring, where they are separated in two beam traveling in the opposite direction and are accelerated to an astonishing 6.5 TeV per beam, causing them to go as fast as 99.999999% of the speed of light.
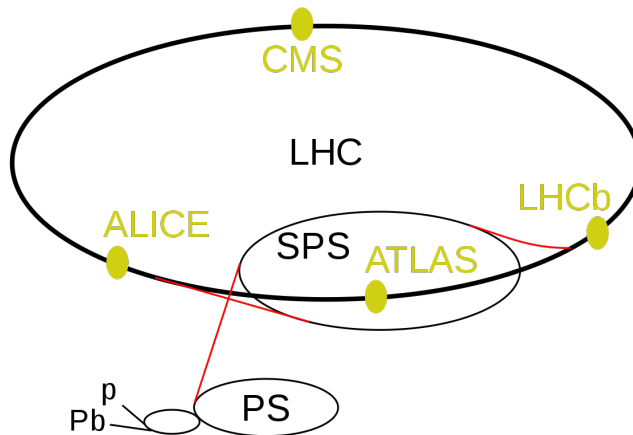
Fig. 2.4. Drawing depicting the main accelerator on the LHC.

2.3.2. Main Detectors at LHC

The LHC has four main experiments taking place on the main ring, ATLAS, CMS, LHCb and ALICE. From these four main experiments, ATLAS and CMS are general-purpose experiments to accurately observe any product from the collision, LHCb is designed to accurately detect the production of b quarks and the ALICE experiment is designed for heavy ion collisions.

The ATLAS and CMS experiments have similar purposes, but dramatically different detector configurations and designs. Being the main topic of this work, the ATLAS detector will be described in section 2.4 while the other detectors are presented hereafter.

CMS

The Compact Muon Spectrometer (CMS) Detector is a general purpose detector to observe every product of proton-proton collisions. The apparatus is 29m long and 15m in diameter [**18**]. Figure 2.5 shows a representation of the CMS detector [**19**]. In its most central part is a silicon tracker, to reconstruct the trajectories of the product of the collision. Around this tracker is the electromagnetic calorimeter (ECAL) to collect particles interacting via the electromagnetic forces, mainly electrons and photons. This subdetector is a homogeneous calorimeter made of $PbWO_4$ scintillating

crystal. Next there is the hadronic calorimeter (HCAL), to capture hadrons. This detector uses the sampling technique with plastic scintillator as active material and brass or steel as absorber. Around the hadronic calorimeter is the superconducting solenoid magnet, used to create a 3.8T magnetic field aligned with the axis of the detector to bend the trajectory of particles. Finally, muon chambers and return yoke are installed outside the magnets, to recapture the magnetic field of the solenoid and bend the tracks of the muons before detecting them.
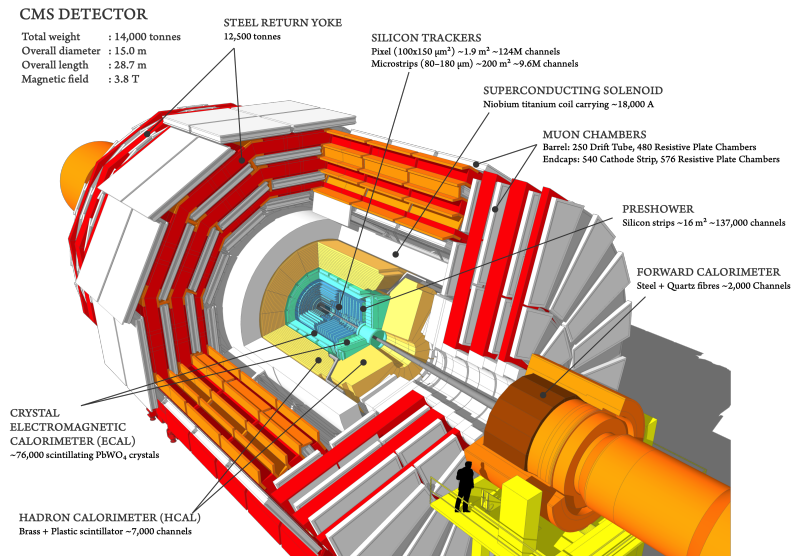
Fig. 2.5. Cutaway diagram of the CMS detector after the Phase 1 Pixel upgrade.

LHCb

Large Hadron Collider beauty (LHCb) is a detector built and designed specifically to observe and characterize events involving b-hadrons (any hadrons containing b quarks) to be able to measure CP-violation in b-hadrons, which could explain the matter-antimatter asymmetry of the universe [20]. Figure 2.6 shows a representation of the LHCb detector [21]. The inner part of the detector is made of a silicon vertex detector (VELO) to measure the primary vertex of the event. Then a first Ring Imaging Cherenkov Detector (RICH-1) is installed for identification of low-momentum particles. Then, a series of silicon and straw tubes tracking subdetectors are installed on both sides of a dipole magnets to measure tracks and momentum of

incoming particles. Next, a second RICH is installed to identify particles with high-momentum. The following subdetectors are the calorimeters. Both electromagnetic and hadronic calorimeters are sampling calorimeters, with lead and iron as absorber for the ECAL and HCAL respectively. Both calorimeters use plastic scintillators as active material. Finally, muon chambers are installed after the HCAL. They are formed of multiple sections of Multi-Wire Proportional Chambers (MWPC) filled with a gas mixture of $CO_2/Ar/CF_4$.
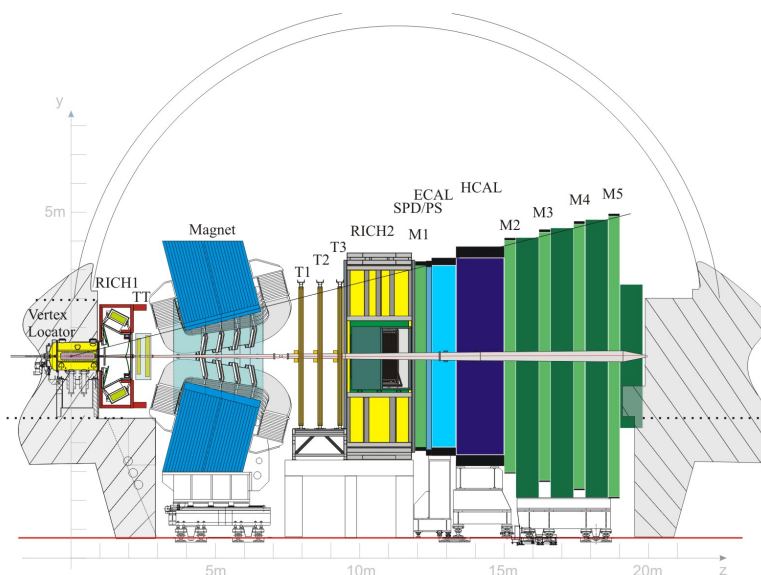
Fig. 2.6. Cross sectional view of the LHCb detector.

ALICE

A Large Ion Collider Experiment (ALICE) is a detector designed to observe the products of heavy ions collisions such as Pb-Pb or Xe-Xe. During such collisions, QCD predicts the creation of a new state of matter called quark-gluons plasma, which is thought to have existed in the first fraction of a second after the big bang. Understanding this new phase of matter would give a much deeper understanding of the first instants of the universe [22]. Figure 2.7 shows a representation of the ALICE detector [23]. The detector is separated into two regions, a barrel region around the axis of the detector and a forward region to observe muons. The inner part of the barrel is the tracking system, made of three subdetectors. First, the Inner Tracking

System (ITS) consisting of three different silicon tracking detectors, then a Time Projection Chamber (TPC), followed by a Transition Radiation Detector (TRD). Following the TRD is the electromagnetic calorimeter and the photon spectrometer, measuring the energy of electrons and photons with high accuracy. These subdetector are embedded in a 0.5 T magnetic field created by a solenoid magnet to bend their tracks. The forward region of the ALICE detector is designed to observe muons. First a thick cone of absorber removes every other particles than muons in the forward region. Muon chambers are placed after the absorber to measure their tracks. A dipole magnet is also installed to be able to measure muons momentum.
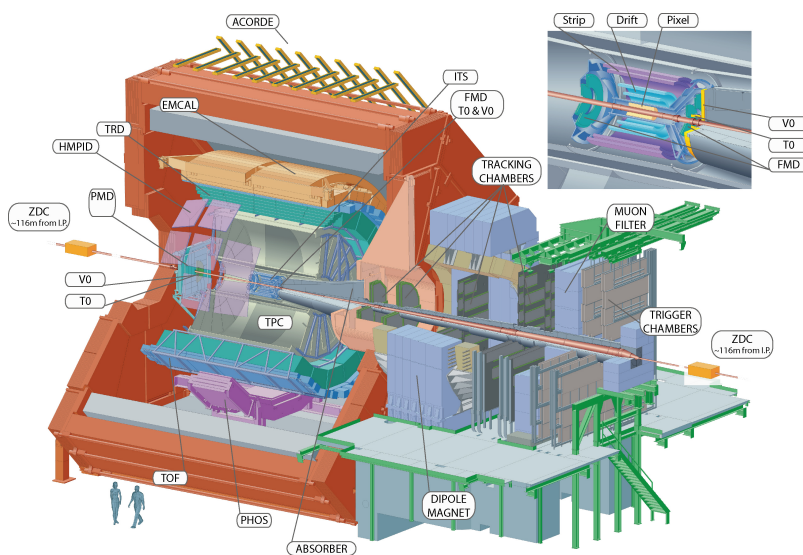
Fig. 2.7. Computer generated cut-away view of ALICE showing the 18 detectors of the experiment.

2.4. ATLAS

A Toroidal Lhc ApparatuS (ATLAS) is a general purpose detector designed to detect the products of proton-proton collisions at 13 TeV [**24**]. The detector is approximately 44 m long and 25 m in diameter. Figure 2.8 show a representation of the ATLAS apparatus [**25**]. The detector is radially segmented in various subdetectors, that will be described in the following subsections. Due to the cylindrical geometry

of the ATLAS detector, every subdetector, except for one, are separated into two regions: central barrels and end-cap disks.

Toroid magnets
Muon chambers
Solenoid magnet
Semiconductor tracker
Transition radiation tracker
Pixel detector
LAr electromagnetic calorimeters
LAr hadronic end-cap and forward calorimeters
Tile calorimeters
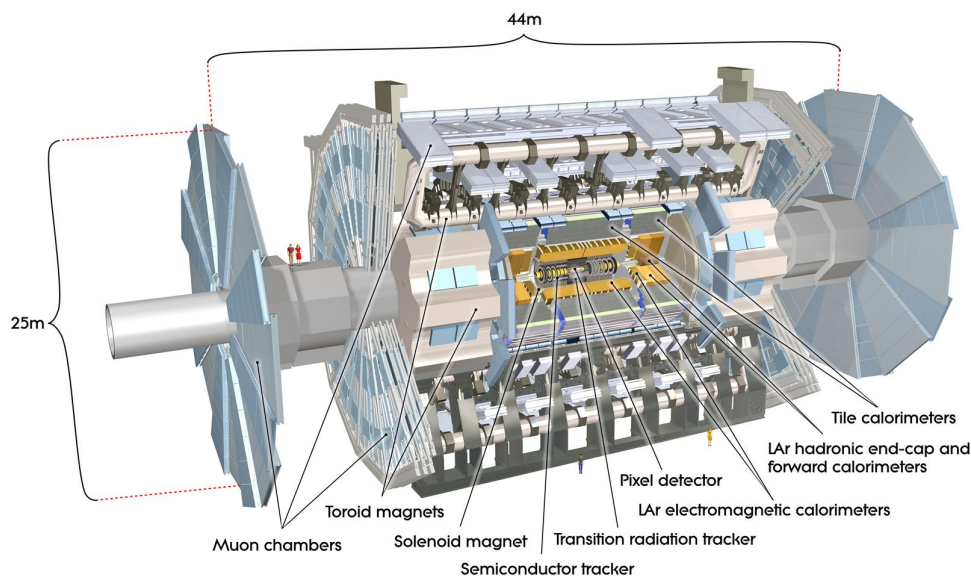
Fig. 2.8. Computer generated image of the whole ATLAS detector.

2.4.1. Inner Detector

The Inner Detector (ID) is the tracker of ATLAS, and is separated in four sub-detectors, the IBL, the Pixel, the SCT and the TRT. Each subdetectors giving information about the trajectories of the incoming particles.

Starting from closest to the interaction point is the Insertable B-Layer (IBL) which is a single layer of silicon pixel detector installed at an average radius of 33 mm from the interaction point in 2014 [**26**]. Its main purpose is to increase the capability of the tracking system to identify secondary vertex from decaying particles. The IBL consists of a silicon layer with electrodes with a pitch of 50 μm$\times$250 μm located on top of it to collect the charges left by particles passing through the detector. This is the only subdetector not having an end-cap region.

The following subdetector in increasing radius is the Pixel detector. Similarly to the IBL, the Pixel is a silicon based solid-state tracker [**27**]. It is made of three barrel, and three end-cap disks on each sides covering a total of 1.73 m^2, reaching

a pseudorapidity of $|\eta| \leq 2.5$, where $\eta \equiv -\ln\left[\tan\left(\frac{\theta}{2}\right)\right]$. Each Pixel module have sensors made of 50 μm$\times$400 μm pixels, providing an excellent track resolution.

Next is the SemiConductor Tracker (SCT), another silicon-based solid state tracker, but with a strip layout instead of pixel [28]. The strip shaped electrodes on the sensor are 12 cm long (two 6 cm strips), and are separated by 80μm, which would only tell which strip a particle went through, but not the coordinate along the strip length. To alleviate that, two module are mounted back to back with a small stereo angle between them ($\pm$20 mrad) to provide a 2D measurement. Knowing the position of the module provides a 3D spacepoint for each track. The SCT is separated in four barrel layers and 9 end-cap disks, giving a total of roughly 6.3 million individual channels.

Finally, the outermost subdetector of the ID is the Transition Radiation Tracker (TRT). This detector is separated into a barrel and two endcaps, covering the region $\eta < 2$. The detector is made of 175 424 drift tubes, 52 544 tubes in the barrel and 125 880 radially aligned tubes in the endcaps, each built of an internal anode wire surrounded by a cathode tube with a voltage of approximately 1450 V applied between them [29]. The tubes were designed to be filled with a 70%/27%/3% gas mixture of $Xe/CO_2/O_2$ to have the proper electrical properties for track measurement. This design yields a number of hits per track between 35 and 40, increasing the precision of the ID.

2.4.2. Liquid Argon Calorimeter

The liquid argon calorimeter (LAr) for the ATLAS detector is based on the sampling technique using lead-stainless-steel as absorber and liquid argon as the active material [30]. The geometry of this subdetector is special, as the absorber plates have an "accordion shape" in radial direction, relative to the interaction point. Figure 2.9 show a representation of the accordion shaped geometry of the ATLAS LAR [30]. The advantage of this peculiar shape is that there is no gap in the coverage due to adjacent calorimeter module, as they overlap. This calorimeter is between

1.15 m and 2.25 m from the beam pipe and has thickness to match the depth of electromagnetic showers.
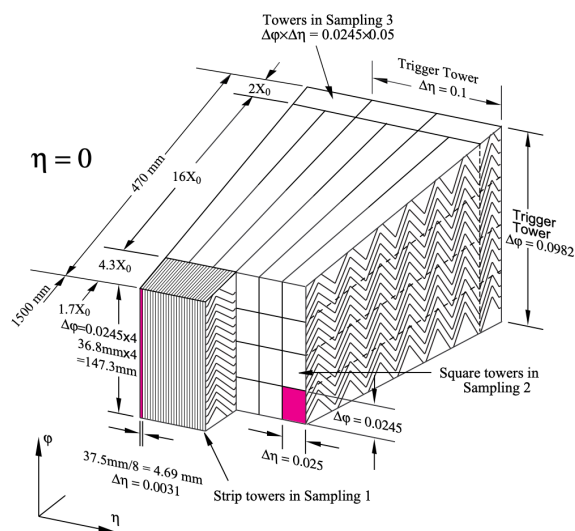
Fig. 2.9. Sketch of the accordion structure of the LAr calorimeter for the ATLAS detector.

2.4.3. Tile Calorimeter

The tile calorimeter for the ATLAS detector is also based on the sampling technique, using steel as absorber and plastic scintillator as active medium [**31**]. The scintillators are readout using wavelength shifting fiber connected radially to photomultiplier tubes (PMTs). The calorimeter is made up of smaller modules called tiles, containing a plate of absorber and a plate of scintillator. These plates are aligned in the R-ϕ plane and staggered radially to have better coverage. The entire subdetector lies between 2.28 m and 4.23 m from the beam axis to contain the entire hadronic shower.

2.4.4. Muon Spectrometer

The muon spectrometer is a tracking detector exclusively for muons, the only charged particle that can be detected past the HCAL [32]. The entire muon spectrometer uses four different detector technologies, two for triggers and two for tracking and momentum measurements. For triggers, the Muon Spectrometer uses resistive plate chambers as well as thin gap chambers. The tracking modules are built using monitored drift tube chambers (MDT) and cathode strip chambers (CSC). For MDTs, three layers of single wire drift tubes are superimposed, giving a position measurement with a $\sim$80 μm resolution. CSCs are multiwire proportional counters, with cathode strips and anode wires perpendicular to each other in a planar geometry. Good resolution is achieved by measuring the charges induced on the cathode strip by the avalanche on the anode wires. In the barrel regions, muon chambers are installed at radii of 5, 7.5 and 10 m from the beam axis making them the last subdetectors of the ATLAS apparatus.

2.4.5. Superconducting Magnets

Superconducting magnets are a crucial part of the ATLAS detector, since they provide the magnetic field necessary to perform momentum measurements of charged particles. There are two magnets used in the ATLAS detector to create a solenoidal field as well as a toroidal field [33].

The Solenoid magnet is placed right outside the Inner Detector. It was designed to create a 2 T magnetic field along the z-axis to curve the track of charged particles in the R-ϕ plane. Figure 2.10 shows a representation of the bare coils of the magnet system [33]. The coil needs to be cooled down to 4.5 K in order for the aluminum coil to be superconductive. To reach the desired magnetic field, a current of 8 kA has to run through the superconducting coil.

The Toroid magnet is separated in two regions, the Barrel Toroid and End-Cap Toroid. The barrel section is made of 8 coils mounted in z-R planes around the beam axis. This magnet is mounted alongside the Muon Spectrometer. The coils generate a field that is almost entirely perpendicular to the track of the particles produced,

wrapping around the detector. The End-Cap Toroids are made of 8 coils similarly to the Barrel Toroid and are mounted on each side of the detector as can be seen in figure 2.10 [33].
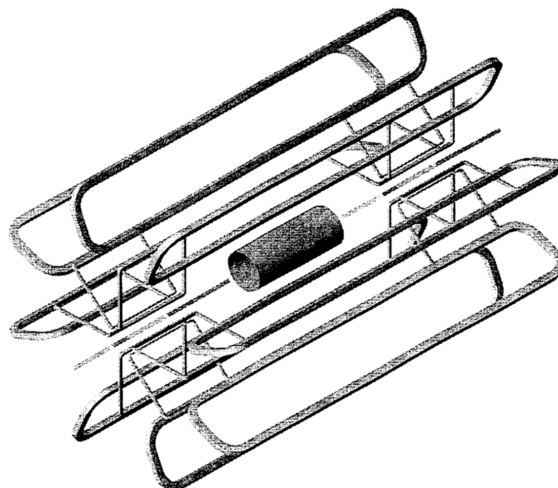
Fig. 2.10. Three-Dimensional view of the bare windings of the ATLAS Magnet System: the Central Solenoid, the 8 coils of the Barrel Toroid and the 2×8 coils of the End-Cap Toroids.

2.5. High-Luminosity LHC

Although the current ATLAS detector has made groundbreaking discoveries in the field of high energy physics, a number of other mysteries are still to be uncovered. With the kind of apparatus as the LHC, two different approaches can be taken to make further discoveries attainable. First, the energy of the LHC can be increased to have access to higher energy processes of the Standard Model and beyond. Another approach is to increase the luminosity of the collider, in order to have enough events to be able to observe rarer processes. The latter approach will be taken by the LHC for 2027, where they will increase their instantaneous luminosity by roughly an order of magnitude (from $\mathcal{L} \approx 1 \times 10^{34} \text{cm}^{-2}\text{s}^{-1}$ to $\mathcal{L} \approx 7.5 \times 10^{34} \text{cm}^{-2}\text{s}^{-1}$ [34]).

This upgrade of the accelerator is called the High-Luminosity LHC (or HL-LHC). With such an upgrade, a significant number of processes will be accessible to study, such as the decay of Higgs to muons ($H \rightarrow \mu^+\mu^-$) [34] or the Higgs self-coupling

(λ_{HHH}) via di-Higgs production [35]. The Higgs' decay to muons will give insight on the coupling of the Higgs boson to different fermions, while the Higgs self-coupling measurement is crucial to establish if the Standard Model Higgs mechanism is responsible for the EW symmetry breaking. Another promising search with the HL-LHC is a resonance in the $t\bar{t}$ production cross-section, caused by a possible new heavy particle at the TeV scale (Z'), decaying to top quarks [36].

All of these searches would only be achievable with to the impressive amount of data that is planned to be produced with the HL-LHC. Unfortunately, more collisions also means more radiation. As a matter of fact, the current ATLAS Pixel detector was designed to withstand a radiation equivalent of around 400 fb^{-1} of integrated luminosity, while the integrated luminosity expected from the HL-LHC is planned to be $\sim$ 4000 fb^{-1}. Moreover, with the increased luminosity, the current ATLAS detector would be saturated and it would directly impact the event reconstruction efficiency.

Hence, because such an upgrade is to be executed for the LHC, the entire ATLAS detector has to be upgraded to sustain the conditions of the HL-LHC, and to be able to make meaningful advancement to the field of high energy physics. This upgrade is called the ATLAS Phase-II Upgrade.

Chapter 3

ATLAS Phase-II Upgrade

The ATLAS Phase-II Upgrade is scheduled during the LHC Long Shutdown 3 (LS3) starting at the end of 2024 until 2027. During these two and a half years, all the subdetectors of the ATLAS detector will be modified or replaced to cope with the new conditions of the HL-LHC. As described in section 2.5, the amount or radiation, as well as the number of events, will be increased roughly by an order of magnitude. Hence, the entire inner detector will be flooded with more events than it can withstand, making the upgrade of the inner detector one of the most important of the entire Phase-II Upgrade. In this chapter, a brief summary of the ITk subdetector will be given in section 3.1. In section 3.2, the ITk Strip detector will be presented, and a brief presentation of the production and testing effort will be given in section 3.3. Finally, one of the most important test for ITk modules, i.e. thermal cycling, will be presented in section 3.4.

3.1. ATLAS Inner TracKer

The ATLAS Inner TracKer (ITk) is the subdetector that will replace the entire Inner detector of the current ATLAS apparatus. The ITk will be an all-silicon semiconductor tracker separated into two subdetector, the ITk Pixel detector and the ITk Strip detector. These two subdetectors will replace the four subdetectors currently installed (IBL, Pixel, SCT and TRT). Figure 3.1 shows a schematic of the entire ITk detector, with the central blue region being the ITk Pixel and outer green region is the ITk Strip detector. The ITk will use the newest semiconductor

tracker technologies to increase the granularity of the detector, while decreasing the amount of material, for better detector precision and efficiency. The ITk Pixel will span roughly twice the radius and four times the length of the current Pixel detector, while the ITk Strip detector will be much more segmented and have three times as much silicon area compared to the previous SCT [34]. Both subdetectors are crucial for the upgraded ATLAS detector to work properly, however, since the work done in the context of this thesis is done exclusively on the ITk Strip detector, the focus of this chapter will be on this subdetector.
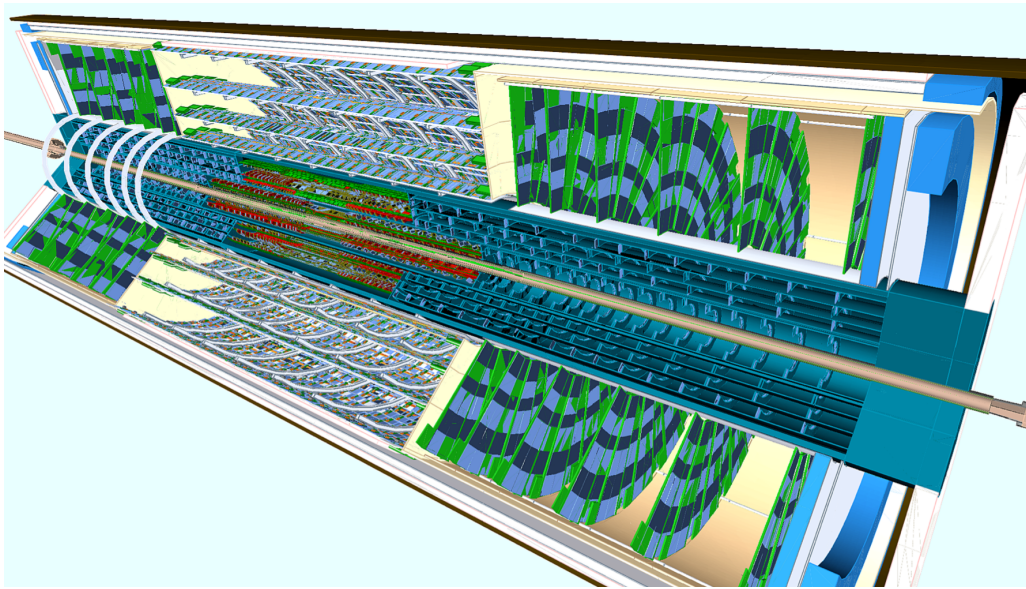
Fig. 3.1. Schematic of a cross section of the ITk detector, with the ITk Pixel detector in blue and the ITk Strip detector in green.

3.2. ITk Strip Detector

The ATLAS ITk Strip detector is made of two different parts, a barrel section comprised of four concentric cylinder surrounding the beampipe at various radii, and an end-cap section with six disks on each side, with detector modules lying in the R-ϕ plane at different distances (z) from the interaction point. The positions of the barrels and disks are optimized to minimize the track parameter resolution and to obtain an approximately constant number of hits on tracks as a function of η

[**34**]. Every layer of the ITk Strip detector is comprised of two sublayers of detector modules, one on each side of the support structure. Figure 3.2 shows a diagram of the layout of the ITk detector, with the Strip detector highlighted in blue [**34**]. In this figure, the barrel and end-cap can easily be identified, as the barrel lies between $z = 0$ mm and $z = 1500$ mm and the end-cap between $z = 1500$ mm and $z = 3000$ mm. One has to note that due to the symmetry of the detector in the z direction, only positive z are shown, but the physical detector will be between $z = \pm 3000$ mm.
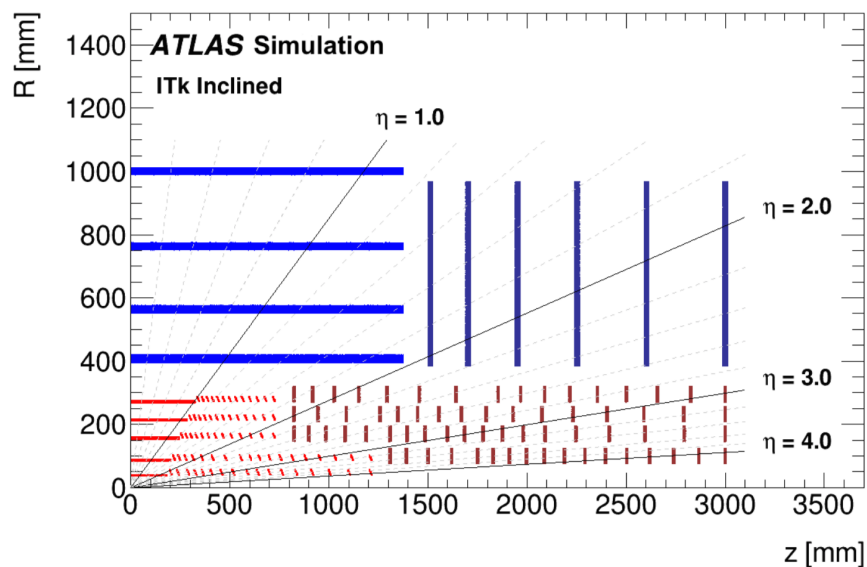
Fig. 3.2. Layout of the ITk detector, with the ITk Pixel highlighted in red and the ITk Strip detector highlighted in blue.

3.2.1. ITk Strip modules

The ITk Strip detector is segmented in numerous modules, varying in size and geometry depending on their position. The entire ITk strip detector will be made of 17 888 modules, 10 976 for the barrel and 6912 for the end-cap. All modules are built in the same way. They are made using 300 μm silicon wafers implanted with conductive strips. On top of the sensor are printed circuit boards (PCBs) mounted with readout chips to collect the data or a power converter to feed the module. These two PCBs are called hybrids and powerboards respectively. The exact geometry depends on where the modules are to be installed. For the Barrel,

modules are rectangular and are covered in strips aligned in the z-direction. The two inner-most layers of the barrels have a strip length of 24.1 mm while the two outer-most layers have a strip length of 48.1 mm. All barrel modules have a pitch of 75.5 μm, which is the distance between the strips. To be able to perform a 3D position measurement, every barrel modules are rotated by 26 mrad compared to the beam axis, giving a total of 52 mrad between pair of modules on a layer. For the Endcap, due to the particular geometry of the detector, the modules have a trapezoidal shape, with two curved edges that are arc of concentric circles centered at the beam axis. Once assembled, these modules cover rings around the beam axis. An end-cap disk is made of six concentric rings (R0 to R5). Figure 3.3 shows a representation of the layout of an end-cap module. The strips on these modules are aligned in the radial direction with length varying between 15.1 mm and 60.2 mm, and with pitch between 71.1 μm and 80.7 μm. These values are not the same for every modules because they depend on which ring the modules belong to. For a 3D position measurement, the strip on the modules are shifted by 20 mrad compared to the radial direction, giving a total of 40 mrad of stereo angle between the modules on each side of a disk. This stereo angle is directly implemented in the geometry of the modules, by aligning the strips with a point slightly off of the beam axis, as is represented on the left part of figure 3.3.
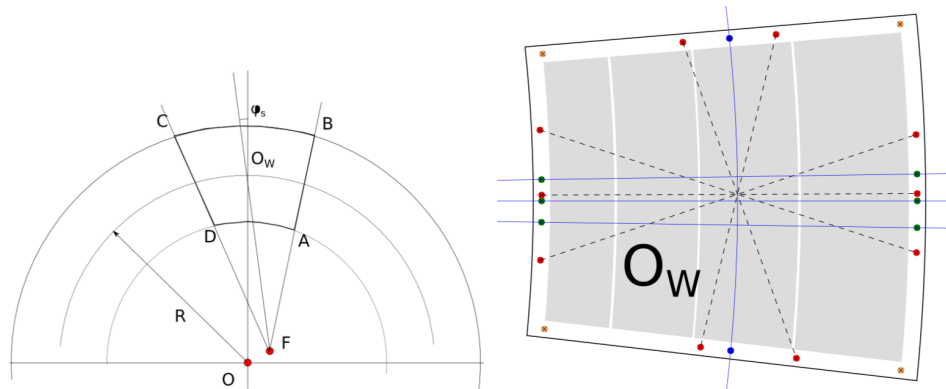

Fig. 3.3. Geometry of an ITk Strip R0 module

To start with, every modules has a silicon sensor made of a 300 μm wafer with strips directly implanted in the wafers. The sensors are produced alongside the

readout chips on the wafer for easier production. The chips are then cut off from the sensor to be mounted on top of it later. For the ITk Strip modules, two different chips, also called Application Specific Integrated Circuits (ASICs), are used to collect and process the data directly on the module. These ASICs are called ATLAS Binary Chips (ABC) and Hybrid Controller Chips (HCC). The former is used to collect the data directly from the strips. Every ABC chips are directly wirebonded to 256 strips on the sensor. Once the data is collected by the ABCs, the data is sent to the HCC to be further processed. These chips are mounted on what are called hybrids, which are PCBs specifically designed to receive these chips. Depending on their geometry, some modules have one or two hybrids, and every hybrid has a single HCC to collect the data from all the ABCs on that hybrid. The second PCB used on the ITk Strip modules are powerboards (PB). These PCBs are designed to receive power from the ATLAS infrastructure and convert it to currents and voltages that can be used by the various chips on the module. The different components of the strip modules are mounted using a thin layer of UV-curing epoxy glue. A first layer is placed between the sensor and the different PCBs (hybrid and powerboard), and the second layer is between the hybrids and the various chips (ABCs and HCCs).

To give the reader a better idea of what an actual ITk Strip End-cap module looks like, a picture of a mechanical R0 module (with dummy, inoperative electronic components) is shown in figure 3.4, where the grey area is the sensor, the green and glass-looking parts are the hybrids and powerboard which are non-functional, and the yellow squares are the positions of the readout chips.

3.2.2. Module Production

Due to the immense size of the ITk project and the various configurations of modules (such as barrel, R0, R1, etc.), several institutions around the world will work towards building the different modules to complete the ITk Strip detector. Because the building procedure has to be extremely precise and consistent, some part of the production of the modules will be done in the industry, since they are already equipped to produce large quantities of the various components needed for
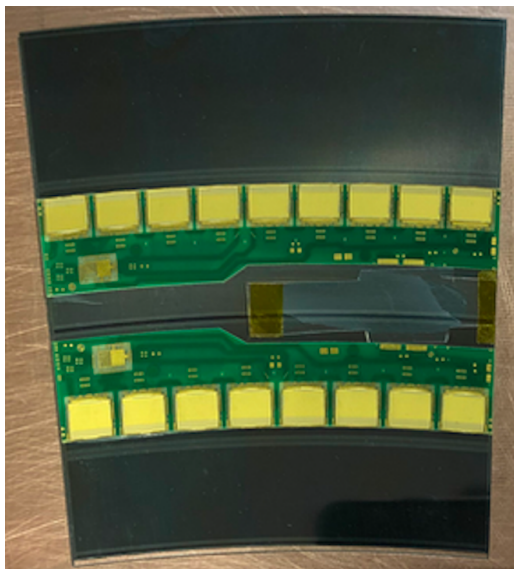
Fig. 3.4. Picture of a mechanical ITk Strip R0 module.

the detector. The exact role of the industry in the production process of modules is different for each institute, but usually, the module components are prepared in the industry, both by company workers and people from an institute. Once fabricated, the components can either be mounted into a module directly by the company using tools designed by the collaboration or shipped to the local institution where the module building will take place. This joint work between institutions and industry will guarantee a high quality and high rate of production to be able to reach production goals.

3.3. Testing

As discussed in section 3.2.1, roughly 20 000 modules will need to be produced (including spares) for the final detector to be installed on the LHC. This huge number is a challenge in itself, paired with the fact that every module has to be working perfectly. Because of that, rigorous and thorough testing procedures need to be defined to assess the quality of the produced components and modules. In this section, a quick overview of the different tests to be performed on modules and components of the ITk strip modules are given. These tests can be separated in

two different categories, namely Quality Control (QC), see section 3.3.1, and Quality Assurance (QA), see section 3.3.2.

3.3.1. Quality Control

A part of the testing procedure is the quality control (QC). These tests will be performed on every components produced. The goal of these test is to make sure that every part produced is of the required quality to be mounted on the modules and later installed on the final ITk detector. This part of testing is crucial because, once installed on the final detector, the modules will be inaccessible for approximately 10 years, since they are located in the innermost region of the ATLAS apparatus. These tests are non-destructive and they assess the quality of the production and the performance of the components. These tests are separated in two categories: the tests done on module components, and afterwards, the tests on assembled modules.

The first series of tests are the reception test, and are done on sensors, powerboards and hybrids, they include visual inspection of packaging and of various shock sensors to make sure that the shipping process did not physically damage the components. Following this inspection, various electrical tests are performed, namely I-V curve on the sensor and electrical confirmation tests of the hybrids and powerboards [37].

If the components of a module pass these tests, they will be mounted on the sensor using the UV-curing glue, and the ABC chips will be wirebonded to the strips on the sensor. During this process, every component is weighted to determine the glue weight and glue coverage of the module. Once everything is mounted, visual inspection of the module is done to assess the quality of the assembly process. Metrology measurements are also made to measure the position of the hybrid and powerboard relative to the sensor. Then, another I-V curve of the sensor is done to look for early breakdown of the module due to glue seepage.

Once the modules are assembled and inspected, the final test done is the thermal cycling. This test is performed to identify premature failure of modules and components by recreating multiple temperature cycles expected in the ATLAS detector.

For the test, the modules are mounted on a specifically designed setup to repeatedly heat them up and cool them down to expected running temperature of the final detector for about 12 hours while doing electrical tests. This test is the cornerstone of this work, thus it will be discussed more in details in section 3.4. If a module doesn't pass one of the previous tests, the components will be recycled if possible, to build other modules. If a module passes every test of QC procedure, it will be shipped to the final assembly facility, where it will later be installed on the ITk infrastructure in the LHC cavern. At these sites, other reception tests will be performed, to make sure the shipping did not damage the modules.

3.3.2. Quality Assurance

The second type of testing is the quality assurance (QA). These tests will be performed on a subset of every module built, on the order of 1%. The goal of these tests is to assess the endurance and reach the limit of the modules and their components. The QA procedure is thus destructive. Here is a list of the various test that will be performed during the QA procedure [37].

- **Irradiation test**: The irradiation test will be performed in several step, until the module stops working. The total irradiation dose has to be much higher than the expected radiation in the final detector during its lifetime.
- **Hybrid/powerboard sheer or peel test**: Force will be applied on the hybrid or powerboard until the glue layer ruptures.
- **Vibration test**: The modules will be vibrated until damage occur.
- **Magnetic field test**: Module will be powered under high magnetic field until they cease working properly.
- **Thermal test**: Module will be heated up until they are non-functional.
- **Thermal cycling**: The modules will be thermally cycled for hundreds of hours (see section 3.4 for a more specific description of thermal cycling).
- **Long term HV stability**: Modules will be powered with high voltage applied, and their stability will be studied.

- **Glue chemical analysis**: Various chemical test will be performed on glue samples to ensure quality and uniformity between batches.

3.4. Thermal Cycling

Thermal cycling is a crucial test for the module because it aims to recreate the extreme conditions that could arise in the final detector. This test is set up to simulate multiple years of working conditions for the modules. This is done by repeatedly heating up and cooling down modules, to recreate the shutting down procedure of the LHC, when cooling facility are turned off. This heating up and cooling down can also occur unintentionally if a major problem happens at the LHC. These test cycles also incorporate tests to assess the state of the modules during the procedure. In the following subsections, a thorough description of the thermal cycling procedure will be presented, the setup used to perform it will also be described, and finally, a challenge of thermal cycling will be discussed, with a solution to mitigate it.

3.4.1. Thermal cycling procedure

The thermal cycling procedure can be separated into three phases. First the preparation for the thermal cycling, then the cycles themselves, and finally an ending phase. A diagram of the thermal cycling procedure is presented in figure 3.5 with the x-axis representing the time elapsed since the beginning of the procedure, and the y-axis representing the temperature of the modules [38]. The major tests done during thermal cycling are also added to give the reader a better understanding of the entire process.

First, the preparation for thermal cycling consists of cooling down the modules to an initial temperature of -35°C during a period of one hour. Once the modules have reached the desired temperature, a series of characterization test are done, such as communication tests with the chips and I-V scans of the sensors to name a few. Once these are done, and the modules are performing correctly, the main part of the thermal cycling can begin.
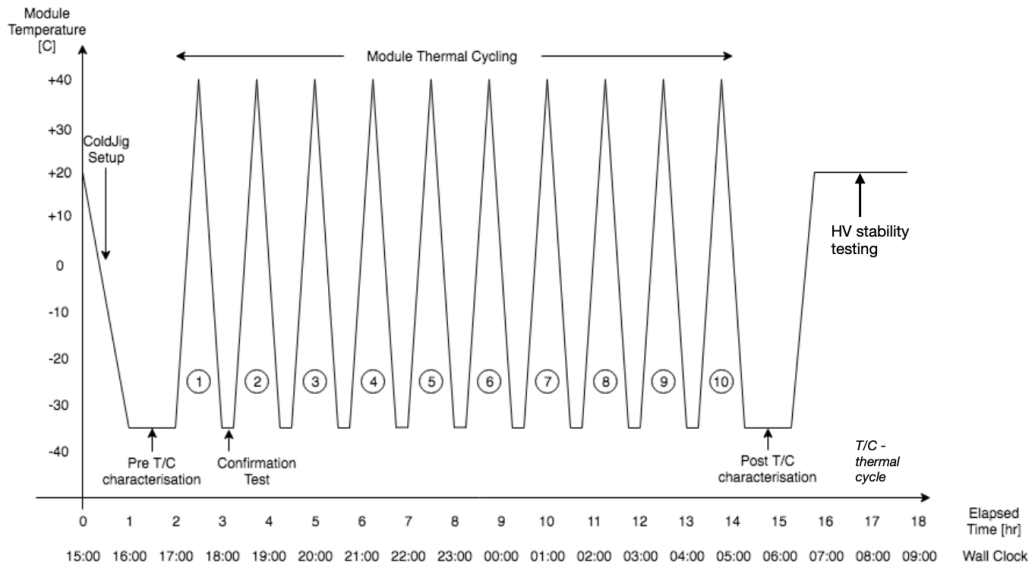
Fig. 3.5. Diagram of the temperature as a function of time for the thermal cycling procedure. The main tests done during thermal cycling are presented.

During a single cycle, the modules are heated up from -35°C to +40°C, and then cooled down once again to -35°C during a period of one hour. At the end of this cycle a series of confirmation tests are done to make sure every module is still working properly. These confirmation tests include a communication tests as well as temperature and current read out. Once these confirmation tests are done, the modules are thermally cycled once again. For the thermal cycling done during Quality Control, a total of 10 cycles will be performed on the modules, while for the quality assurance procedure, the modules will have to withstand on the order of 100 cycles. When the cycles are done, the final part of thermal cycling can start.

Finally, when all cycles are completed, the modules will be tested using the same characterization tests as in the beginning, while the modules are still at -35°C. Once these tests are done, the modules are heated back up to room temperature (20°C) and a final high-voltage stability test is done during the final two hours. During this HV test, the leakage current is monitored, and a module passes if the current stays constant throughout the 2-hour period.

46

Once all the tests are done, the modules that pass the thermal cycling are then sent to the next stage of testing while the modules that fail are sent back in production to be recycled if required.

3.4.2. Thermal cycling apparatus

To perform thermal cycling, a specific setup needs to be used. This setup is called a "coldbox" and it includes all the hardware and electronics needed for thermal cycling. Figure 3.6 shows a picture of a prototype coldbox used for ITk Strip barrel modules. Because the modules are cooled down to -35°C, a sealed insulated box is crucial to keep the inside volume at a low temperature and with very low humidity. To achieve this, a layer of insulating foam is placed inside of a simple metal box. To keep a low humidity level, a gas inlet is added to flush the volume of the coldbox with dry nitrogen, to stay above the dew point and prevent frost formation on the cooled modules. Multiple cables and tubes are also passing through the box to feed coolant, vacuum and power to the testing setup inside. As seen in figure 3.6, the coldbox will contain four or five cooling jigs, which will receive the modules.
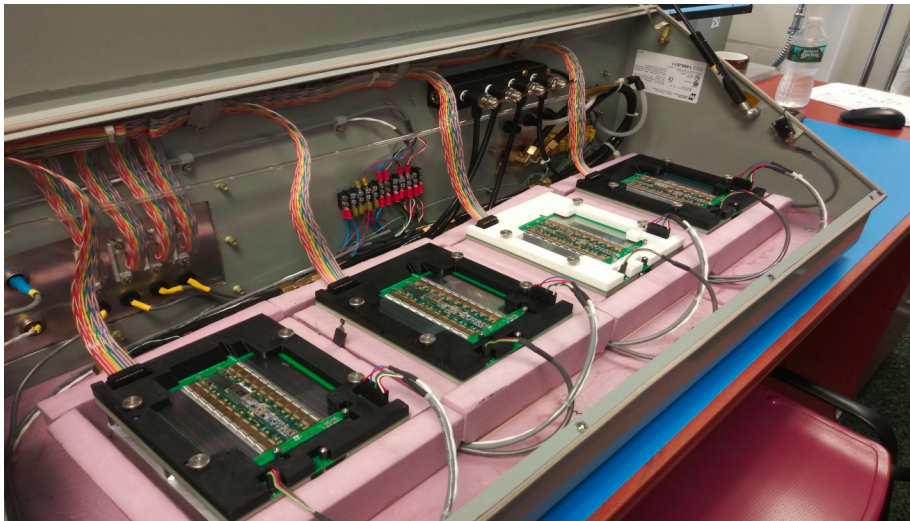

Fig. 3.6. Picture of a prototype coldbox for ITk Strip barrel modules, showing a four-module version.

The cooling jigs consist of aluminum blocks that are machined with an internal pattern to allow for a liquid coolant to flow through them. All the jigs are connected

to an external chiller that circulates the coolant. Another part of the cooling jig is what is called a vacuum chuck, which is also a piece of machined aluminum. This component is machined to have multiple holes in it to allow for a vacuum pump to suck the air out underneath the modules to properly hold them in place. Finally, a third piece of aluminum is added as a support for the module and the necessary electronics. A schematic of the jigs is shown in figure 3.7 with the three main parts highlighted.
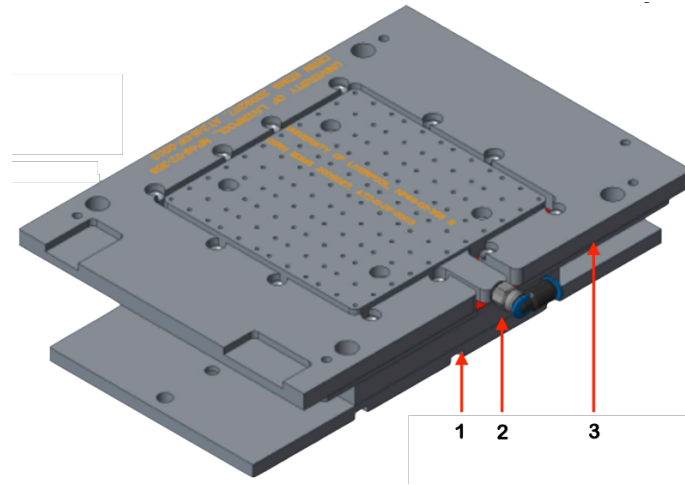
Fig. 3.7. Schematic of the cooling jigs, with the three main parts numbered (1-cooling block, 2-vacuum chuck, 3-Test frame support).

On top of the cooling jig is placed what is called a module test frame, which component is a sheet of printed circuit board populated with the necessary electronics to power a module. The test frame also has a central part which has exposed copper and thermal vias to have a good thermal conductivity between the cooling jig and the module. A schematic of the test frame is shown in figure 3.8. One can notice the blue region in the central part of the test frame, which is the region with exposed copper. Also in this region are multiple holes in the test frame to communicate the vacuum to the module placed on top, hence holding it in place. Finally, the modules are placed on top of the test frame. They are aligned and partially held in place with a polymer transport frame that is placed on top of the modules, as seen in figure 3.6.
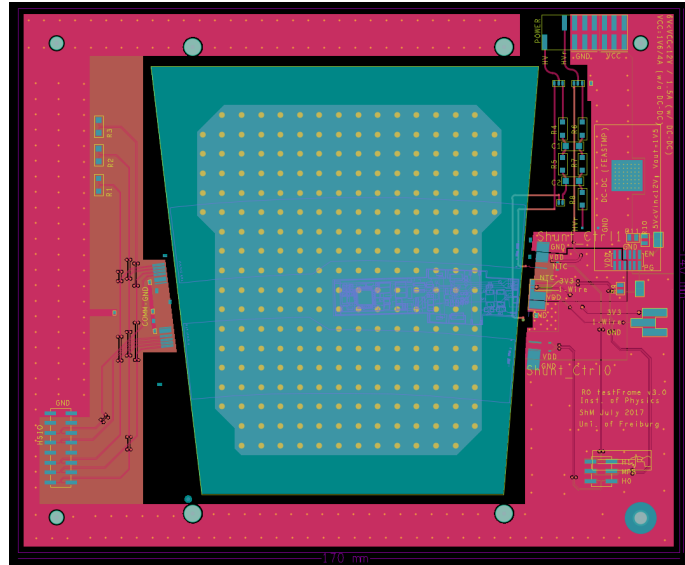
Fig. 3.8. Schematic of the test frame for R0 modules.

Once assembled, the temperature and humidity of the environment, as well as the modules themselves are monitored using a computer with a software designed specifically for the coldbox. This software has multiple interlock implemented to shut down the high voltage applied on the module and terminate the thermal cycling if anything goes wrong. The humidity level in the coldbox have to be monitored closely because if any moisture enters the coldbox while the modules are cooled down, frost form and damage the modules.

3.4.3. Thermal cycling challenges

Due to the harsh conditions it creates, thermal cycling poses a lot of challenges for the modules. The main problem encountered during thermal cycling preliminary tests is that, due to differences in thermal expansion coefficient of the materials used in the modules, the latter tends to bend when cooled down, thus potentially breaking the vacuum holding it in place durint the testing phase. Because this bending cannot be mitigated due to its intrinsic nature, a solution had to be found to maintain the vacuum for the whole duration of the tests. One idea raised during the R&D phase of the design of the coldbox is to add a thin rubber-like seal between the module and the test frame, which would prevent the vacuum from breaking even if the module bends.

Although this idea solves the vacuum problem, it brings other issues. For example, the small layer added by the seal will cause the module to deform when vacuum is applied because of the atmospheric pressure on top. This new mechanical strain thus induces new internal forces in the module. In the context of continuum mechanics, these internal forces are represented by what is called stress. To make sure this new procedure has no chance of damaging the module, a careful investigation was done to assess the level of stress created in the module by this new seal idea. The results of this investigation are presented in the following chapter, as it is the main part of this thesis.

Chapter 4

Stress Evaluation of ITk Strip Module During Thermal Cycling

Because thermal cycling is one of the most important test both in quality control and quality assurance of the ITk Strip Modules, it is important to understand and quantify the stress felt by the modules during this procedure, to make sure to identify faulty module and remove them before they are installed. In this chapter, results from Finite Element Analysis simulation computing the stress created in the sensors of ITk Strip modules during thermal cycling will be presented. First, in section 4.1, a quick introduction to Finite Element Analysis will be given. Next, the software, procedure and materials used for the simulations will be described in section 4.2. Finally, the results from this study will be presented in section 4.3.

4.1. Finite Element Analysis

The simulations done in the context of this work use Finite Element Analysis (FEA). It is a numerical method used in engineering, physics and mathematics to solve various problems, such as wave propagation, fluid dynamics and heat transfer to name a few. The basic idea of FEA is to separate the domain over which the solution has to be computed into small discrete regions called finite elements, where the solution can be computed more easily. In the context of this work, the way the domain is separated is called a mesh, where the complicated geometries are replaced with multiple small polyhedrons (tetrahedrons or prisms). Once the mesh

is defined, boundary conditions representing the physics of the problem are defined on the geometry, and the FEA software solves the predefined equations representing the underlying physics over the finite elements. The results over the finite elements are then combined to give a global solution over the entire geometry [**39**]. To perform the simulations described in this work, the COMSOL Multiphysics™software version 5.3a [**40**] was used.

4.2. Analysis

In this section, the software used for the FEA simulation as well as the various steps done to reach the results of the stress in the sensor due to our thermal cycling setup are described.

4.2.1. Software

In the context of this work, the software used to perform the FEA simulation is *COMSOL Multiphysics™*. This software is a cross-platform software specifically engineered to solve coupled systems of partial differential equations for various physics and multiphysics problems. Our group at Université de Montréal acquired a license of the software as well as the following packages needed to create and run those simulations: The *CAD Import* module [**41**] to be able to import the files containing the 3D model of the modules, test frame and vacuum seal and the *Structural Mechanics* module [**42**] to be able to use the *Solid Mechanics* physics as well as the *Heat Transfer in Solid* physics. The *Solid Mechanics* module gives access to all mechanical constraints needed for the simulation, such as fixing a part of the geometry in space, and applying a force or pressure on certain region of the model, while the *Heat Transfer in Solid* gives access to applying temperature constraints on the model. While using both of these modules, COMSOL also gives the opportunity to use the *Multiphysics* interface, granting the access to the *Thermal Expansion* physics, which is one of the main source of deformation in this work.

The *COMSOL Multiphysics™* uses predefined equations representing the physics to solve, and solves these coupled equations over the domain defined by the simulation

with the boundary conditions defined by the user. For the purpose of Structural mechanics, the equation solve is given by equation 4.2.1

$$\boldsymbol{\nabla} \cdot (FS) + \mathbf{F}_v = 0 \tag{4.2.1}$$

Where S is the second Piola-Kirchhoff stress tensor, F is the deformation gradient defined as $F = 1 + \nabla \mathbf{u}$ where u is the deformation field, and $\mathbf{F}_v$ is an external force applied to the system. In the case of thermal expansion, the equation used to describe this phenomenon is presented in equation 4.2.2.

$$F \rightarrow (1 + \epsilon)F \tag{4.2.2}$$

Where F is still the deformation gradient, and ϵ is the thermal expansion, given by $\epsilon = \alpha(T)(T - T_{ref})$, where $\alpha(T)$ is the temperature-dependent thermal expansion coefficient, and T_{ref} is the reference temperature, at which we consider no thermal expansion. With these equation defined, *COMSOL Multiphysics*^{TM} can solve them and give a result of the final deformation and stress of the specified geometry, given proper initial conditions.

4.2.2. Procedure

The following steps were performed in order to reach valid conclusions regarding the stress caused by thermal cycling.

- The first step was to simulate the cooling of an R0 modules, free in space, to have a first reference value for the stress. As a boundary condition for this simulation, a point was fixed in space for the simulation to be able to converge properly. For this simulation the side of the powerboard was fixed, so it would not affect the stress in the sensor. For the cooling, a temperature condition was applied on every boundary of the geometry, starting from room temperature down to -30°C. This simulation was also compared to a similar simulation done by a colleague at DESY [43]. The goal is to have similar results to be able to confirm that our simulating environment is correctly set up.

- The following step in the study was to add the test frame with our vacuum seal in the simulation. The new geometry contains the R0 module, as well as the test frame with the vacuum seal. In this simulation, only the vacuum was applied, to see its effect on the stress induced in the sensor. To apply the vacuum, a boundary load was added on the part of the module that lies inside the vacuum seal. This boundary load was a force per unit area (i.e. a pressure) with a value of 101.3 kPa. For the simulation to converge properly, the pressure was applied in increasing steps, solving the simulation for every intermediate value and using this solution as a first estimate of the following step, until the final value was reached. This procedure is called an auxiliary sweep. To fix the geometry in space, the metal layer on the backside of the test frame was fixed.

- After the vacuum, the cooling/heating of the entire geometry was added to the simulation. The same heating/cooling method as the free module was used, while keeping the vacuum and the fixed boundary condition. In this part, two different simulations were used, because it is assumed that the modules are built without any intrinsic stress in them, and that the temperature at which they are built is room temperature. Thus, to correctly represent that, one simulation was done for the cooling (from $+20°C$ to $-35°C$) and another for the heating ($+20°C$ to $+40°C$). In these simulations, an auxiliary sweep was also used for the pressure. The values of stress then computed were compared to the value computed with only the vacuum applied. This comparison was done to see only the effect of the cooling/heating on the module due to our thermal cycling setup.

- The next step was to see the effect of the thickness of the vacuum seal on the stress induced in the module, without the cooling or heating. To do such a simulation, the geometry itself had to be parametrized, varying the seal thickness to the desired value for each simulation. This was done using a parametric sweep, which means that a simulation is computed for every input value of the parameter, in this case from 15 μm to 75 μm in 5 μm increments.

An auxiliary sweep was also used for the pressure in this simulation for easier convergence. The same fixed boundary condition and pressure condition as the "vacuum only" simulation were used.

- Another simulation that was done was one where a loss of vacuum was simulated. The purpose of this simulation was to see how would the stress would vary if the vacuum was lost on some part of the module. To perform that simulation, the pressure applied on the modules was removed only on the upper 10mm, which simulates a loss of vacuum on that part of the sensor. Once again, an auxiliary sweep was used for the applied pressure.

- The final step of this study was to create a simulation of an R0 module glued to a hard structure, to mimic the layout of the final detector. In that case, no vacuum was applied, and the standard cooling procedure was used. The results of this simulation are then compared to the results of the simulation on the thermal cycling setup, to check how the stress endured during normal operation conditions compares to thermal cycling.

4.2.3. Materials

Once the geometry is well defined for a simulation, materials have to be assigned to each part to simulate the proper physical properties. Every material used in the simulations are described in table 4.1, with their associated domains. It is important to note that the materials used are the same for every simulations done for this study. Because COMSOL Multiphysics™ has a built-in material library, all the materials below were imported from this library.

4.3. Results

4.3.1. Free Module

The goal of this simulation was to have a reference value for the stress in the sensor. This reference is the stress felt by a module cooled down from $+20°C$ to $-30°C$ while being free in space.

Tab. 4.1. Summary of the materials used for the FEA simulation of the ITk R0 module during thermal cycling.

Entity	Domain	Material	% V/V	Comment
R0 module	Sensor backplane	Aluminum	100 %	Only for a 2D layer
	Sensor	Silicon	100 %	Single-crystal, isotropic
	Hybrid-sensor glue	HYSOL FP4526	50 %	Epoxy-style glue
		Silicone	50 %	-
	Hybrids & PB[1]	Polyimide	92 %	-
		Copper	8 %	-
	ASIC-hybrid glue	Same as Hybrid-sensor glue		
	ASICs	Silicon	100 %	Single-crystal, isotropic
Test frame	Test frame bulk	FR4	100 %	Composite material-
	Test frame metal layer	Copper	100 %	-
	Vacuum seal	Silicone	100 %	-
Petal config-uration	Petal glue layer	Same as Hybrid-sensor glue		

[1]The ratio of copper to polyimide used here was chosen to take into account the metal connections of the electronics in the polyimide matrix of the PCB.

After being imported into COMSOL Multiphysics™, the geometry of a free R0 module was modified to remove minor problems, such as redundant faces and smalls edges, to have a proper 3D model of a module. Once the changes were applied, the geometry shown in figure 4.1 was achieved. This geometry is inspired from the requirement of the R0 module from the ATLAS ITk Strip module Technical Design Report except that the power-board is not populated with the proper hardware and some of the electronic components on the hybrid were left out, such as the HCC, for a simpler model. These changes are not expected to affect the results for the stress

in the sensor [**44**], but will significantly decrease the computing time necessary to simulate the whole geometry, from multiple hours to less than an hour per simulation.
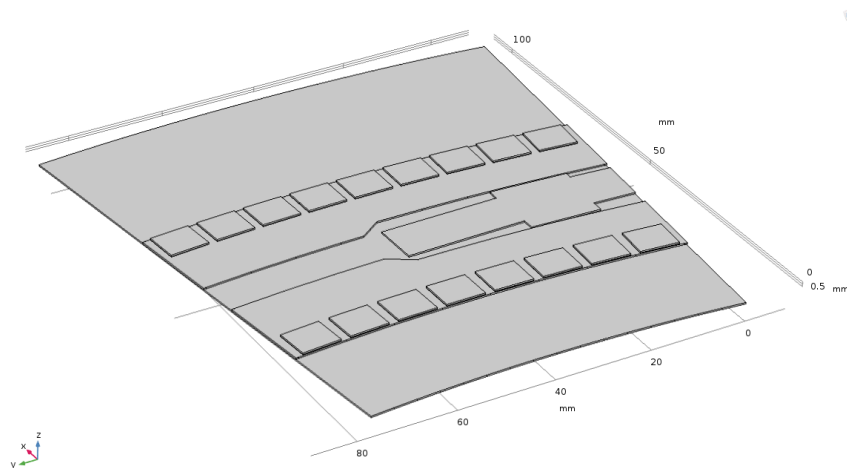

Fig. 4.1. Geometry of the ITk End-Cap Strip R0 module as seen from the COMSOL Multiphysics™GUI.

A simulation was already done of this exact process by a different group [**45**]. Their results, shown in figure 4.2, are used as a reference to make sure that the simulating environment of this work is properly setup. The goal is thus to have similar results.

For our simulation, there were some details that were different compared to the reference simulation. For example, the glue properties used were updated to represent a more realistic composition of the glue, which affects the simulation quite a lot, as can be seen in figure 4.3. In fact, the distribution of stress changes significantly between our simulation and the reference, but the maximum value, which is more interesting for the purpose of this study, is approximately the same for both simulations (i.e. 25 MPa for the reference and ~26 MPa for ours.).

4.3.2. Thermal Cycling Setup: Vacuum only

An important part of this work was to simulate the test frame that will be used to receive the R0 modules for testing. This test frame, a piece of FR4 which is a glass-reinforced epoxy laminated material, with the necessary electronics to power and
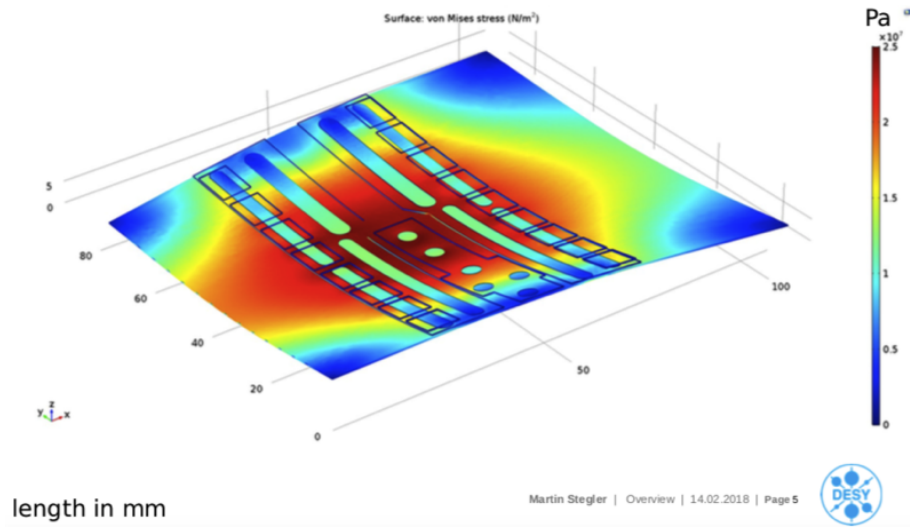
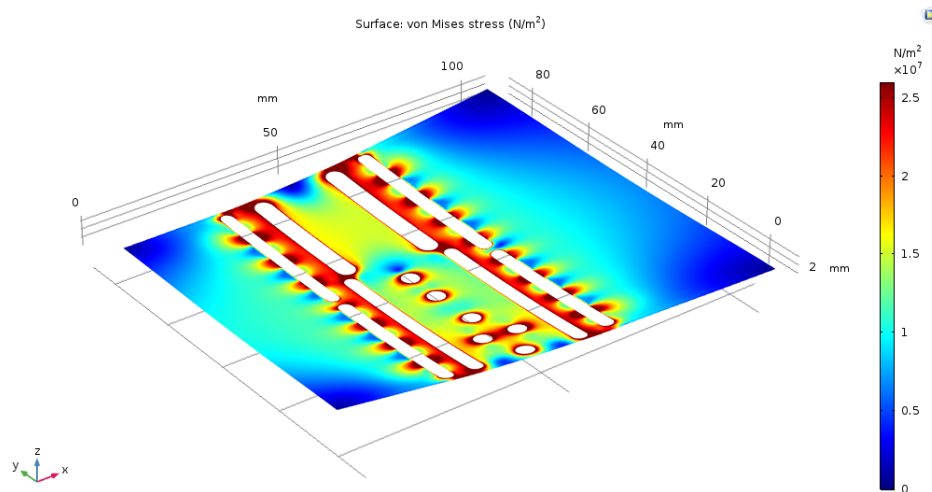**Fig. 4.2.** Reference simulation of the stress distribution in a free R0 module due to the cooling from $+20°$C to $-30°$C.

Fig. 4.3. Stress distribution in a free R0 module due to the cooling from $+20°$C to $-30°$C.

read-out the module [46], was already designed. The frame geometry was simplified to get rid of a lot of unimportant details for the purpose of the FEA simulations that would have caused the computation time to become too long for the computing power available. All of the electronics on top of the frame were removed, and only the central part was left (a thin metal layer for thermal contact). It is important to

note that the removal of the small details should not noticeably affect the results. Another important part of the test setup for the thermal cycling is the vacuum seal. The seal is a simple deposited silicone layer, applied directly on the surface of the test frame. In real life, the goal is to apply that layer using a specially designed injection machine controlled by a computer, that can reach thickness down to a few tens of microns. Thus the chosen thickness for the seal is set to 50 μm, to minimize the curvature of the module when placed on the seal as much as possible. This seal was added because during some test performed at DESY, it was reported that the vacuum was lost for unknown reasons, and the shock caused by the loss of vacuum fractured the sensor of a test module. Following that, a vacuum seal was designed to make sure that vacuum loss does not happen during the module testing procedure. The geometry of the test frame with the vacuum seal can be seen in figure 4.4.
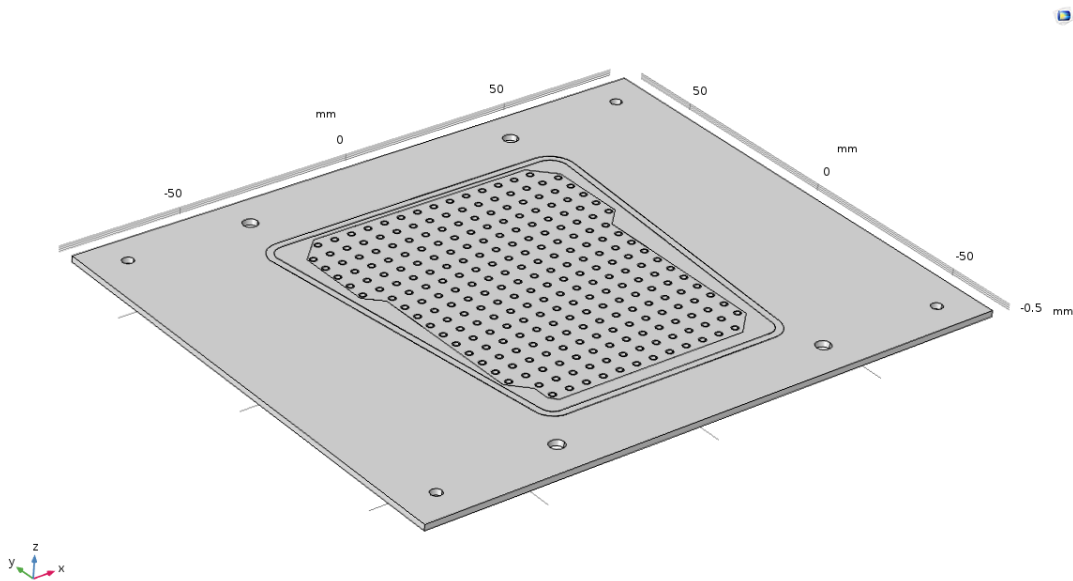

Fig. 4.4. Geometry of the test frame after all the details were removed and the vacuum seal was added as seen from the COMSOL Multiphysics™GUI.

The following simulation was done to see the effect of the seal paired with the vacuum on the stress in the module. For this simulation, the geometry used contains the R0 module as well as the test frame and the vacuum seal described previously. This geometry can be seen in figure 4.5. For most of the following simulations, this

59

geometry is untouched; the placement of the seal doesn't change, the metal layer on top of the frame is fixed at 3.5 μm and the seal thickness is set to 50 μm.
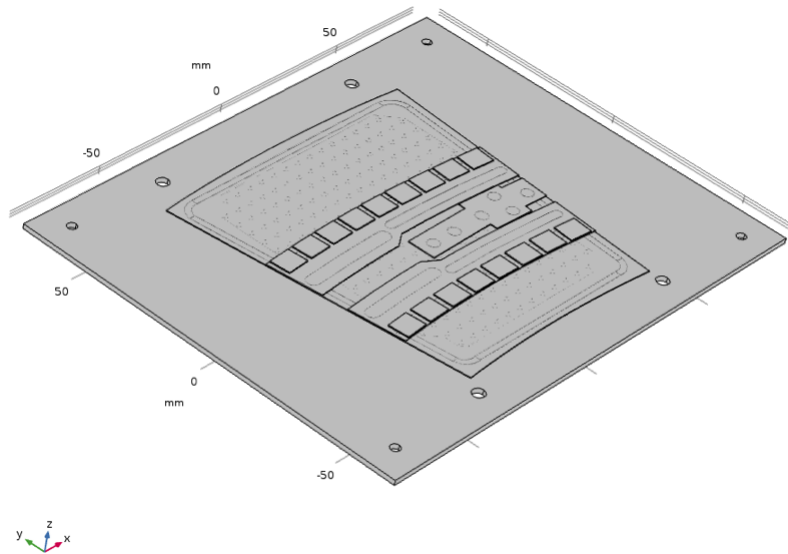

Fig. 4.5. Geometry of the final setup, containing the ITk End-Cap Strip R0 module on top of the test frame with the vacuum seal, as seen from the COMSOL Multi-physics™GUI.
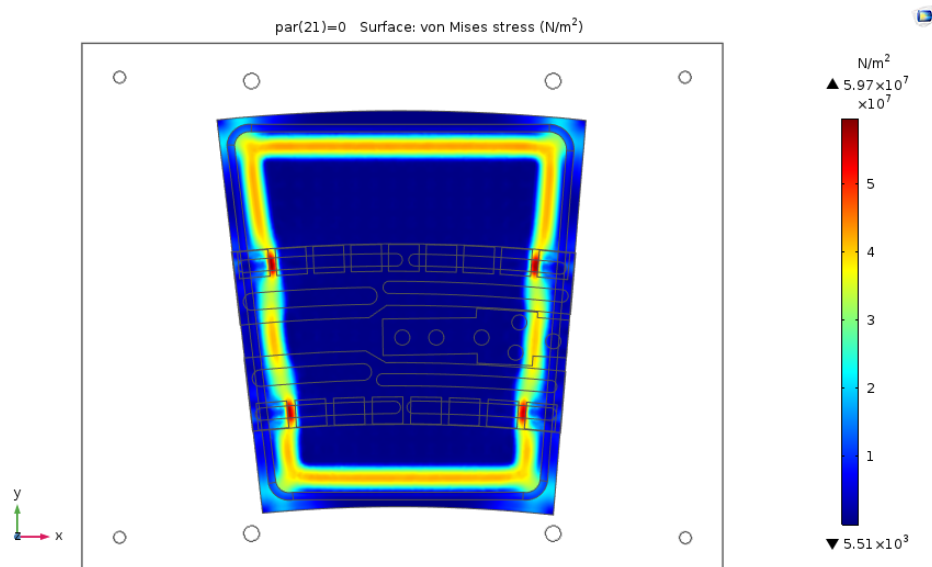

Fig. 4.6. Stress distribution in the sensor of an R0 module on the Test Frame due to the vacuum applied with a 50 μm vacuum seal.
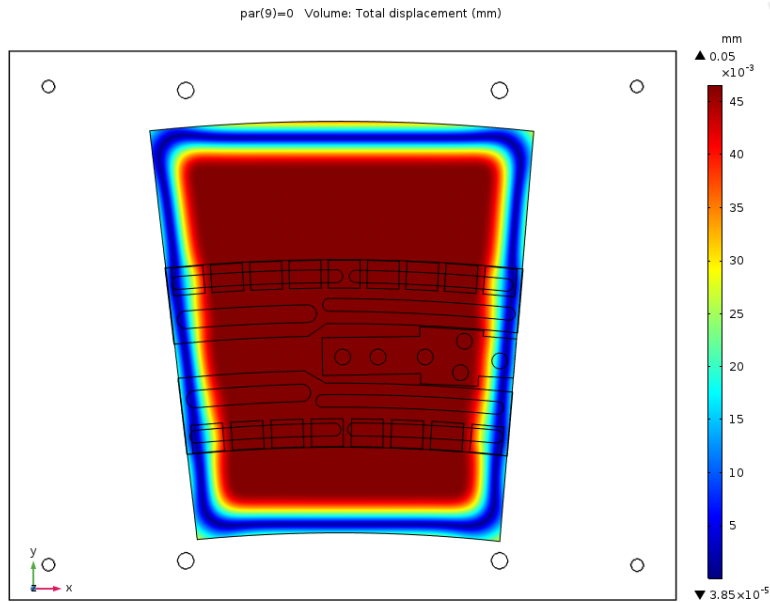
Fig. 4.7. Displacement of the sensor of an R0 module on the Test Frame due to the vacuum applied with a 50 μm vacuum seal.

As it can be seen in figure 4.6, the highest stress in the module with only the vacuum applied appears in the region where the module bends to lie flat on the top of the test frame. This can also be seen in figure 4.7, which shows the displacement of the sensor from its original position. This plot shows that the central part of the sensor moved downwards by about 46.5 μm, that represents the initial height of the module (50 μm) minus the height of the metal layer of the test frame (3.5 μm) on which the module sits after the vacuum is applied.

Other than the trapezoid shape of the stress distribution, one can observe in figure 4.6 four red spots that correspond to regions with higher stress than their surroundings. These four regions corresponds to where the bending regions of the module meet the layer of hybrid-to-sensor glue. At these four points, the maximum stress value is 59.7 MPa, which is about three times higher than the maximum stress for a cooled free R0 module. This is a first indication of the importance of the seal with the vacuum in creating stress in the module.

4.3.3. Thermal Cycling Setup: Cooling/heating

The following simulation was done to see the effect of the cooling and heating of the module in the thermal cycling setup on the induced stress in the sensor. This simulation uses a similar framework than the previous simulation, but this time, a cooling/heating condition was added to the geometry, in a similar fashion to the simulation of the cooled free R0 module. The results for the cooling simulation are shown in figure 4.8, and for the heating simulation in figure 4.9.
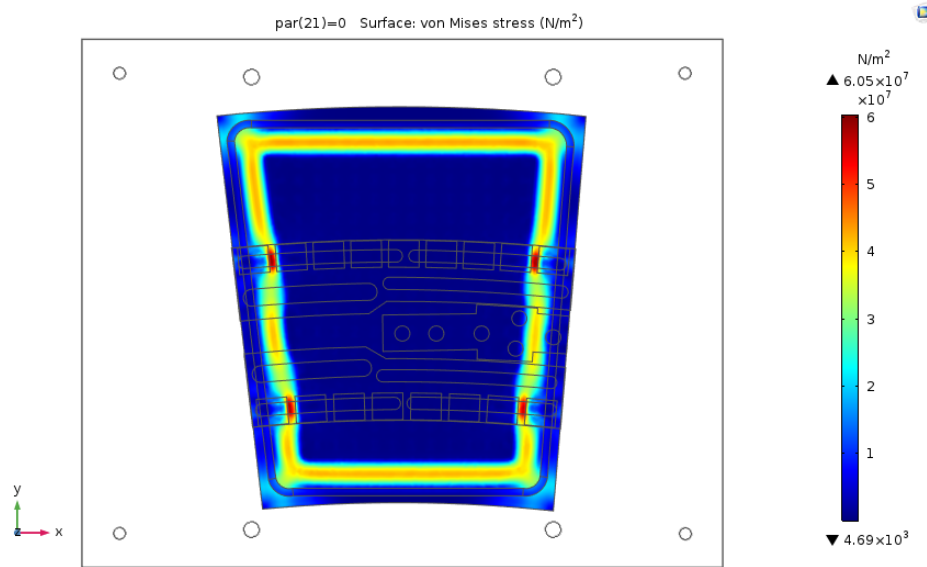

Fig. 4.8. Stress distribution in the sensor of an R0 module on the Test Frame due to the cooling from $+20°$C to $-35°$C and the vacuum applied with a 50μm vacuum seal.

For the cooling simulation, the result is compared to the stress presented in figure 4.6, and one can observe that the stress pattern is exactly the same, there still is the trapeze shape, and the four high stress regions are still present. The main difference is the maximum stress value, which is 60.5 MPa, compared to 59.7MPa for the vacuum only simulation. This result can be explained because the cooling process is forcing the center of the module to bend downward, as seen in the results of section 4.3.1. For elastic deformation, stress is proportional to strain (deformation), so the cooling
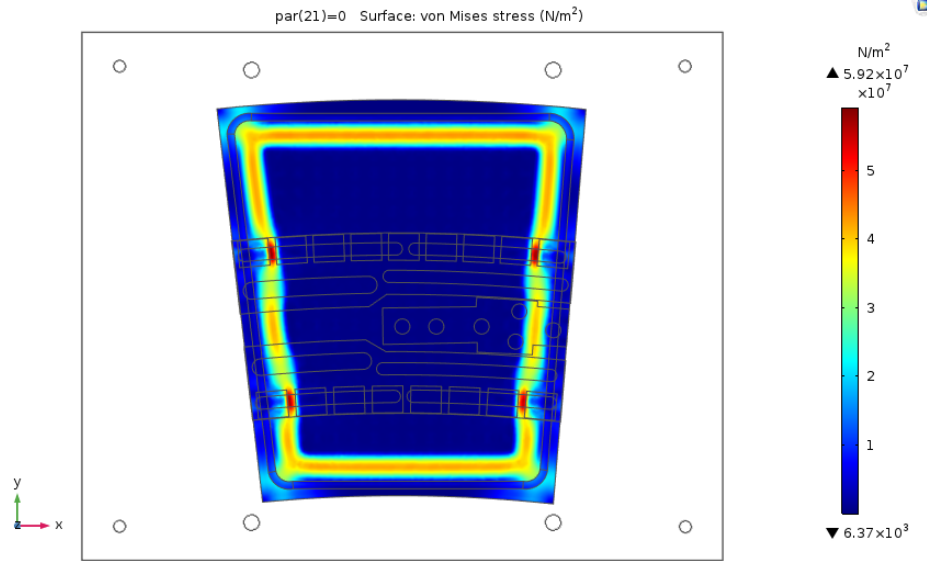
Fig. 4.9. Stress distribution in the sensor of an R0 module on the Test Frame due to the heating from +20°C to +40°C and the vacuum applied with a 50μm vacuum seal.

process actually works in the same way as the pressure for bending the module, thus increasing the strain, which in turns increases the stress.

For the heating simulation, comparable results as the cooling simulation can be seen, except for the maximum value of stress, which decreases for the heating, i.e. 59.2 MPa compared to 59.7 MPa. A similar explanation can be used to describe the decrease in stress, with the exception that if the module is heated, the center tends to bend upward instead of downward, and will thus work against the vacuum.

With the previous results, we can conclude that the most important source of stress in the module during the thermal cycling test will be the seal with vacuum applied, and not the cooling and heating themselves. Because the values of stress computed with the cooling/heating are not significantly different from the ones calculated from the vacuum only simulation, it was decided not to take into account these processes for the rest of the study. This decision was taken because it would decrease the amount of computing resources needed for each subsequent simulation by approximately half.

4.3.4. Thermal Cycling Setup: Seal Thickness

The following simulations were done to see the effect of the vacuum seal thickness on the stress in the module. These simulations use the same framework as the vacuum only simulation presented in section 4.3.2. The only change made was the addition of a parametric sweep to see the stress induced in the sensor as a function of the seal thickness. For this simulation, the seal thickness was varied between 15μm and 75 μm by increment of 5 μm. The results can be seen in figure 4.10.
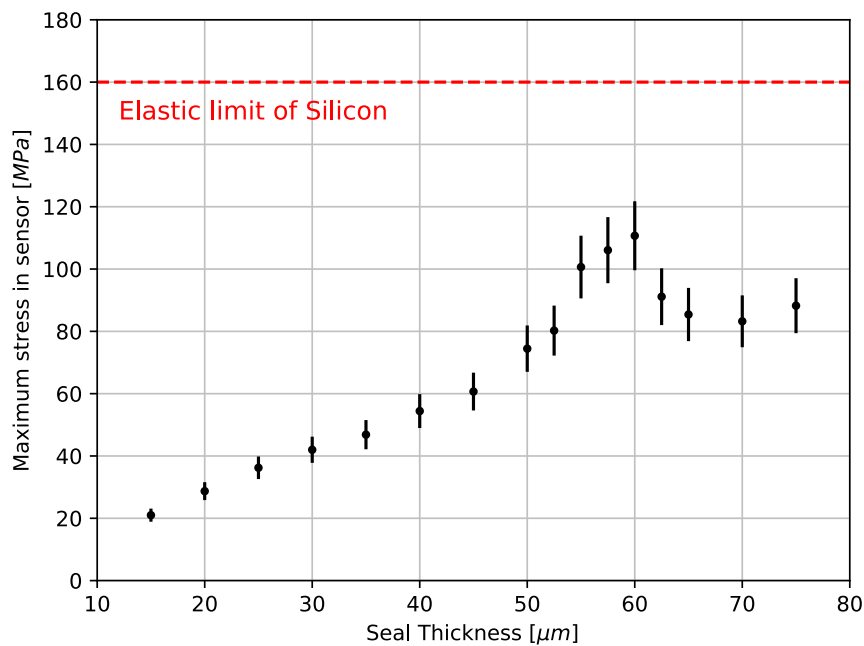
Fig. 4.10. Maximum stress induced in the sensor on the thermal cycling setup due to vacuum as a function of the vacuum seal thickness. The error bars shown were calculated using the tolerance of the simulations

To start with, one can notice that the general behavior of the maximum stress in the sensor as a function of the seal thickness is approximately linear. This behavior is expected because the higher the seal is, the more curvature the sensor has to have to lie flat on top of the test frame, and stress is proportional to strain, in this case, curvature. One can also notice a bump in the maximum stress for seal thicknesses

between 50 μm and 65 μm. This behavior is not well understood since, after an inspection of the stress distribution for these thicknesses, no artifact was present and the regions of maximum stress were still the same regions as described in section 4.3.2. To understand this behavior, a deeper investigation should be done, to uncover the reason of this stress bump for these particular thicknesses. Finally, the elastic limit of silicon is shown as the red dotted line in figure 4.10. The elastic limit represent the maximum stress at which deformation in the silicon will cause permanent change in the structure of the crystal. One can notice that even with the unknown bump in the maximum stress, the values stay well below this limit, and thus should not affect the structure of the sensor. Unfortunately, even though the elastic limit of silicon is known, this value is an ideal superior limit of the tolerable stress, because we do not know how the maximum tolerable stress is affected by the different components and glue layer of the module. Thus a maximum stress well below the elastic limit should be aimed.

From the previous results, we can then conclude that the maximum stress in the sensor during thermal cycling is affected by the thickness of the vacuum seal, and that in general, the thinner the seal, the less stress the module would be subjected to. The seal thickness should then be chosen in such a way that the stress in the module would be as close as possible to the expected stress on the final petal configuration of the modules, while staying well below the elastic limit of silicon.

4.3.5. Thermal Cycling Setup: Vacuum Loss

The following simulation was done to see the effect of the loss of vacuum during testing on the stress in the sensor. To simulate vacuum loss, the applied pressure representing the vacuum was simply removed on the upper part of the module. The result for this simulation is shown in figure 4.11.

For this simulation, one can observe that the stress pattern is very similar to the simulation presented in figure 4.6, for the vacuum only, with the exception that the stress on the upper part of the sensor is decreased by about 10 MPa. Also, the region with maximal stress are decreased by a very small amount ($\sim$0.4 MPa).
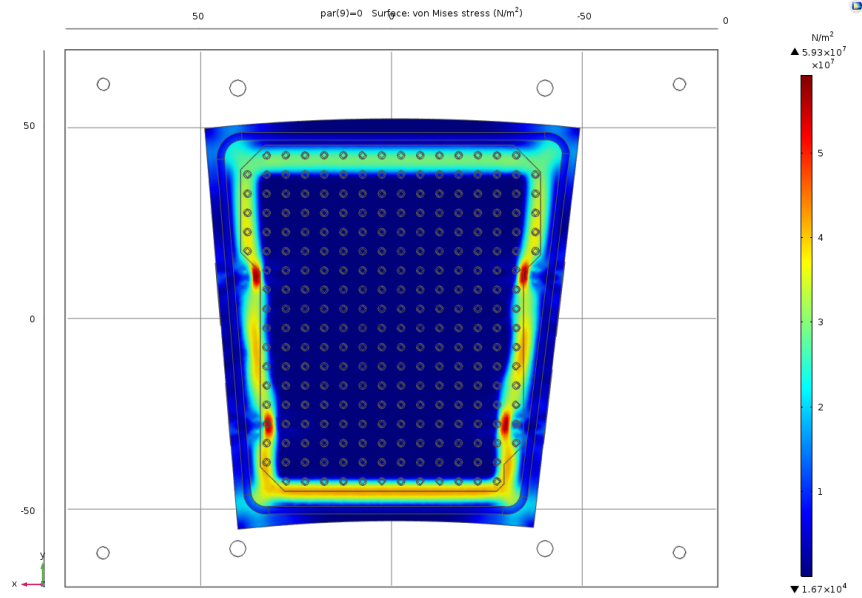
Fig. 4.11. Stress distribution in the sensor of an R0 module on the Test Frame due to vacuum with a simulated vacuum failure on the upper 10 mm section of the module.

Unfortunately, this simulation is inconclusive because the simulation solved for a stationary state, meaning that the transition from a perfect vacuum to the faulty vacuum was not simulated. Nonetheless, this problem could be addressed in the future by computing a time-dependent simulation, to see the evolution of the stress to make sure that it would not possibly break the module.

4.3.6. R0 Final geometry

For the final simulation, a geometry similar to the final detector needed to be created. On the final detector, the modules will be glued onto a flat structure, called a Petal. To recreate this layout, the geometry is based on that of the free R0 module, described in section 4.3.1, simply another glue layer is added on the back of the module, to represent the module-to-petal glue. A thickness of 200 μm was selected to match the other glue layers of the module. The geometry can be seen in figure 4.12.
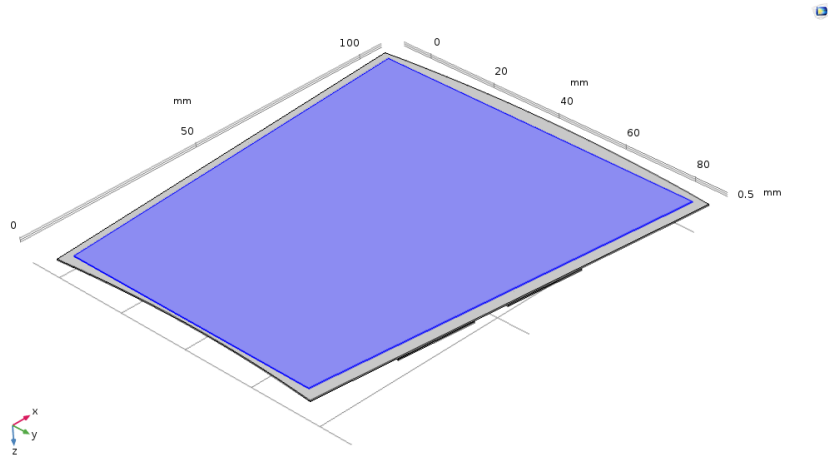
Fig. 4.12. Geometry of the R0 module with the module-to-petal glue (blue) seen from below, from the COMSOL Multiphysics™GUI.

The following simulation was done to see the effect of the cooling process on the stress in the sensor, if the module is in a layout similar to the final detector. The procedure for this simulation is similar to that of the free R0 Module. The result for this simulation is shown in figure 4.13

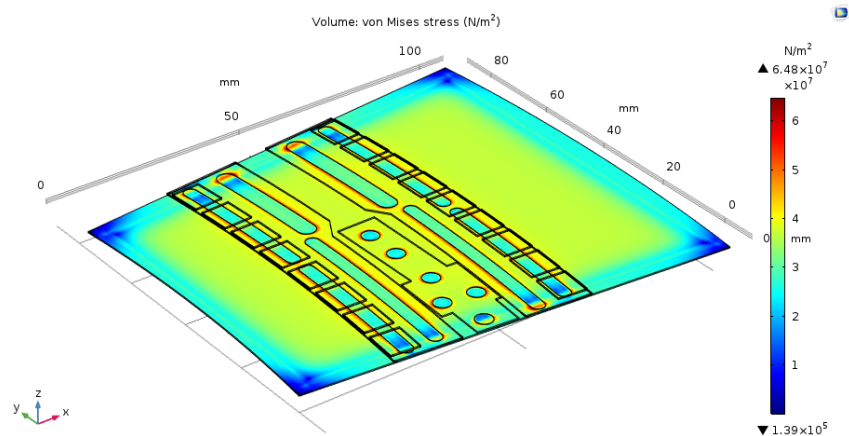**Fig. 4.13.** Stress distribution in the sensor of an R0 module in a configuration close to the petal, while being cooled down from $+20°$C to $-35°$C.

As it can be seen, the stress distribution is fairly uniform over the center of the sensor, which is expected due to the glue layer on the back side of the module, which constrains the displacement of the sensor. The regions where the stress is

higher correspond to where the sensor is in contact with the glue layer connecting the sensor with the hybrids and the powerboard. In these regions, the maximum value of stress is 64.8 MPa, which is really close to the value computed for the R0 module mounted on the test frame for the thermal cycling. With these result, we can conclude that the stress felt by the sensor in a geometry close to the final detector is in the same order of magnitude to that felt in our thermal cycling setup, and that a seal of approximately 50 μm is well suited to simulate the stress of the final detector.

From the simulations presented in this chapter, we observed a stress of approximately 26 MPa for a free ITk Strip R0 module when cooled down from $+20°$C to $-30°$C. We can also conclude that the stress felt by an ITk Strip R0 module during thermal cycling is mainly caused by the vacuum applied to keep the module in place, since the maximum stress changes by less than 1.5% from the vacuum only case, when cooling or heating is included. After an investigation of the effect of the seal thickness on the stress created in the module, we can conclude that a thicker seal would cause a greater stress, as expected. Even considering this behavior, the maximum stress caused by the seal in the range of thicknesses aimed by this study is still at least a factor 2 below the elastic limit of silicon. Vacuum failure was also investigated in this chapter, but due to its dynamic nature, no valid conclusion could be reached by our stationary simulations. Finally, the maximum stress felt by a module in a layout similar to the final detector was computed, producing a value of 64.8 MPa, which is really close to our thermal cycling setup with a seal thickness of 50 μm (59.7 MPa). We can then conclude that our setup is a good layout to perform the thermal cycling test, because the conditions created in this layout is very close to that of the final detector, which is the main goal of the thermal cycling test.

Conclusion

The work presented in this master's thesis was in the context of the upgrade of the ATLAS detector at CERN. After giving a quick introduction to the Standard Model of particle physics, an overview of the present and future particle detectors around the LHC ring was given, as well as the basic principles making them possible. Because of the tremendous size of the upgrade of the ATLAS detector and its inner tracker, the ATLAS ITk detector, a rigorous testing procedure was defined to assess the quality of production. One of the most important test of this procedure is the thermal cycling of detector modules, because it is designed to reenact the conditions of the final detector. During thermal cycling, detector modules are heated up and cooled down, which induces stress, but the level of stress induced was unknown until this study. Because vacuum is used to hold the modules in place on the thermal cycling setup, paired with a vacuum seal to make sure no leakage occurs, a new source of stress was added, which is caused by the module bending due to the vacuum applied. In this work, Finite Element Analysis was used to quantify the stress in the sensor of ITk Strip module to make sure no damage can occur while thermally cycling the detectors.

In light of this study, several conclusions were reached. First, it was observed that the stress in a free module when cooled down to -30°C was around 25 MPa, which is consistent with another simulation done of the same system. Moreover, during thermal cycling of module, the stress is mostly due to the vacuum applied to keep the module in place. As seen from the results from section 4.3.3, the maximum stress in the sensor when only the vacuum is applied reaches 59.7 MPa, while the stress only reaches 60.5 MPa and 59.2 MPa when cooling and heating are considered,

respectively, which makes vacuum the most important source of stress while thermal cycling. Moreover, the maximum stress felt by the module during thermal cycling is highly dependent on the thickness of the vacuum seal used as seen from section 4.3.4. From these results, one can notice that a thinner seal would cause a significantly lower stress. Vacuum failure was also investigated, but the results were inconclusive because of the dynamic nature of vacuum failure, thus a time-dependent simulation should be done to investigate this situation. Finally, with the results shown in section 4.3.4, the stress felt by the module in our thermal cycling setup would be between 20 MPa and 100 MPa. If these values are compared to the stress in the sensor of a module in a layout similar to that of the final detector, with a maximum around 64.8 MPa shown in section 4.3.6, we can conclude that our setup is a good layout to perform the thermal cycling test, because the stress in both situations are of the same order. Unfortunately, at the time of writing this thesis, the decision of removing the vacuum entirely from the thermal cycling setup was made by the collaboration, due to the complexity of adding a seal deposition step in the production procedure and the fact that the thermal contact between the module and the cooling setup was sufficient without vacuum to reach the desired temperature. Despite this decision, the results reached in this study are still relevant because they proved that the stress induced by heating and cooling is not threatening the structural integrity of the modules.

Bibliography

[1] MissMJ, "Elementary particles included in the standard model." `https://commons.wikimedia.org/w/index.php?curid=4286964`.

[2] L. Wolfenstein, "Neutrino oscillations in matter," *Phys. Rev. D*, vol. 17, pp. 2369–2374, May 1978.

[3] M. Tanabashi *et al.*, "Review of particle physics," *Phys. Rev. D*, vol. 98, p. 030001, Aug 2018.

[4] S. Bilenky, J. Hošek, and S. Petcov, "On the oscillations of neutrinos with dirac and majorana masses," *Physics Letters B*, vol. 94, no. 4, pp. 495 – 498, 1980.

[5] LHCb Collaboration, "Observation of a narrow pentaquark state, $P_c(4312)^+$, and of the two-peak structure of the $P_c(4450)^+$," *Phys. Rev. Lett.*, vol. 122, p. 222001, Jun 2019.

[6] M. Thomson, *Modern Particle Physics*. Cambridge University Press, 2013.

[7] ATLAS Collaboration, "Standard Model Summary Plots Spring 2019," Tech. Rep. ATL-PHYS-PUB-2019-010, CERN, Geneva, Mar 2019.

[8] D. Nomura and T. Teubner, "Hadronic contributions to the anomalous magnetic moment of the electron and the hyperfine splitting of muonium," *Nuclear Physics B*, vol. 867, no. 2, pp. 236 – 243, 2013.

[9] G. Ross and R. Roberts, "Minimal supersymmetric unification predictions," *Nuclear Physics B*, vol. 377, no. 3, pp. 571 – 592, 1992.

[10] F. Zwicky, "Die Rotverschiebung von extragalaktischen Nebeln," *Helvetica Physica Acta*, vol. 6, pp. 110–127, 1933.

[11] G. Bertone and D. Hooper, "History of dark matter," *Rev. Mod. Phys.*, vol. 90, p. 045002, Oct 2018.

[12] S. P. Martin, "A Supersymmetry primer," pp. 1–98, 1997. [Adv. Ser. Direct. High Energy Phys.18,1(1998)].

[13] *https://www.researchgate.net/figure/Particle-content-of-the-minimal-supersymmetric-standard-model-There-are-three$_f$ig2₂37008550.*

[14] ATLAS Collaboration, "Summary plots from the atlas supersymmetry physics group." `http://atlas.web.cern.ch/Atlas/GROUPS/PHYSICS/CombinedSummaryPlots/SUSY/`.

[15] Sgbeer, "Linear accelerator for elementary particles with drift tubes.." `https://en.wikipedia.org/wiki/File:Lineaer_accelerator_en.svg`.

[16] B. Vachon, "Phys-620b: Experimental technique in high energy physics," *(Course on experimental techniques in High Energy Physics given at McGill University, Montréal)*.

[17] A. Horvath, "The lhc experiments and the preaccelerators.." `https://en.wikipedia.org/wiki/Large_Hadron_Collider#/media/File:LHC.svg`.

[18] CMS Collaboration, "CMS Physics: Technical Design Report Volume 1: Detector Performance and Software," tech. rep., Geneva, 2006.

[19] "Sectional view of the cms detector.." `https://cms.cern/news/cms-detector-design`.

[20] LHCb collaboration, "Framework TDR for the LHCb Upgrade: Technical Design Report," Tech. Rep. CERN-LHCC-2012-007. LHCb-TDR-12, Apr 2012.

[21] "Lhcb subdetector structure.." `http://lhcb-public.web.cern.ch/lhcb-public/Images2018/LHCbUpgrade.jpg`.

[22] K. Aamodt *et al.*, "The ALICE experiment at the CERN LHC," *JINST*, vol. 3, p. S08002, 2008.

[23] Pcharito, "Schematics of the alice subdetectors.." `https://commons.wikimedia.org/wiki/File:2012-Aug-02-ALICE_3D_v0_with_Text_(1)_2.jpg`.

[24] ATLAS Collaboration, "The ATLAS Experiment at the CERN Large Hadron Collider," *JINST*, vol. 3, p. S08003, 2008.

[25] J. Pequenao, "Computer generated image of the whole ATLAS detector." https://cds.cern.ch/record/1095924, Mar 2008.

[26] A. La Rosa, "The ATLAS Insertable B-Layer: from construction to operation," *JINST*, vol. 11, no. 12, p. C12036, 2016.

[27] G. A. et al, "ATLAS pixel detector electronics and sensors," *Journal of Instrumentation*, vol. 3, pp. P07007–P07007, jul 2008.

[28] J. Jackson, "The atlas semiconductor tracker (sct)," *Nuclear Instruments and Methods in Physics Research Section A: Accelerators, Spectrometers, Detectors and Associated Equipment*, vol. 541, no. 1, pp. 89 – 95, 2005. Development and Application of Semiconductor Tracking Detectors.

[29] ATLAS TRT Collaboration, "The ATLAS Transition Radiation Tracker (TRT) proportional drift tube: design and performance," *JINST*, vol. 3, p. P02013, 2008.

[30] ATLAS Collaboration, "ATLAS liquid argon calorimeter: Technical design report," tech. rep., 1996.

[31] ATLAS Collaboration, "ATLAS tile calorimeter: Technical design report," tech. rep., 1996.

[32] ATLAS Collaboration, "ATLAS muon spectrometer: Technical design report," tech. rep., 1997.

[33] ATLAS Collaboration, "ATLAS magnet system: Technical Design Report, 1," tech. rep., Geneva, 1997.

[34] ATLAS Collaboration, "Technical Design Report for the ATLAS Inner Tracker Strip Detector," Tech. Rep. CERN-LHCC-2017-005. ATLAS-TDR-025, CERN, Geneva, Apr 2017.

[35] ATLAS Collaboration, "Study of the double Higgs production channel $H(\to b\bar{b})H(\to \gamma\gamma)$ with the ATLAS experiment at the HL-LHC," Tech. Rep. ATL-PHYS-PUB-2017-001, CERN, Geneva, Jan 2017.

[36] ATLAS Collaboration, "Study on the prospects of a $t\bar{t}$ resonance search in events with one lepton at a High Luminosity LHC," Tech. Rep. ATL-PHYS-PUB-2017-002, CERN, Geneva, Feb 2017.

[37] S. Wonsak, "Module qa/qc overview." `https://indico.cern.ch/event/837485/contributions/3548268/attachments/1907684/3159135/FDR-Module-QA-QC-overview.pdf`.

[38] A. Mitra, "Module thermal cycling." `https://indico.cern.ch/event/837485/contributions/3548272/attachments/1907727/3159402/ModuleThermalCycling_FDR_20Sep19.pdf`.

[39] D. L. Logan, *A First Course in the Finite Element Method*. CL Engineering, 2011.

[40] COMSOL Inc., "Comsol multiphysics reference manual version 5.3a." `http://www.comsol.com/`, 1998–2017.

[41] COMSOL Inc., "Cad import module user guide version 5.3a." `http://www.comsol.com/`, 1998–2017.

[42] COMSOL Inc., "Structural mechanics user guide version 5.3a." `http://www.comsol.com/`, 1998–2017.

[43] M. Stegler, "Fea & maximum stress measurements." `https://indico.cern.ch/event/702656/contributions/2885611/attachments/1599543/2535414/PDR_14-02-18.pdf`.

[44] J.-F. Hiller, "Private communication," *COMSOL Inc Representative*.

[45] T. Affolder, I. Bloch, B. Hommels, C. Klein, J. Kroll, M. Mikestikova, A.-l. Poley, M. Stegler, and Y. Unno, "Investigation of the impact of mechanical stress on the properties of silicon strip sensors," Dec 2017.

[46] F. Nechansky, "R0 test frame design." `https://twiki.cern.ch/twiki/bin/view/Main/QualTask`.